Published for SISSA by Springer

Received: *August 6, 2024*
Revised: *February 13, 2025*
Accepted: *March 13, 2025*
Published: *May 16, 2025*

Monte Carlo studies of quantum cosmology by the generalized Lefschetz thimble method

Chien-Yu Chou and Jun Nishimura

KEK Theory Center, Institute of Particle and Nuclear Studies,
High Energy Accelerator Research Organization,
1-1 Oho, Tsukuba, Ibaraki 305-0801, Japan
Graduate Institute for Advanced Studies, SOKENDAI,
1-1 Oho, Tsukuba, Ibaraki 305-0801, Japan

E-mail: ccy@post.kek.jp, jnishi@post.kek.jp

Abstract: Quantum cosmology aims at elucidating the beginning of our Universe. Back in early 80's, Vilenkin and Hartle-Hawking put forward the "tunneling from nothing" and "no boundary" proposals. Recently there has been renewed interest in this subject from the viewpoint of defining the oscillating path integral for Lorentzian quantum gravity using the Picard-Lefschetz theory. Aiming at going beyond the mini-superspace and saddle-point approximations, we perform Monte Carlo calculations using the generalized Lefschetz thimble method to overcome the sign problem. In particular, we confirm that either the Vilenkin or the Hartle-Hawking saddle point becomes relevant if one uses the Robin boundary condition depending on its parameter. We also clarify some fundamental issues in quantum cosmology, such as an issue related to the integration domain of the lapse function.

Keywords: Cosmological models, Models of Quantum Gravity, Stochastic Processes

ArXiv ePrint: 2407.17724

https://doi.org/10.1007/JHEP05(2025)142

Contents

JHEP05(2025)142

1 Introduction

Quantum cosmology is a fascinating subject, which aims at elucidating the beginning of our universe. In early 80's, two important ideas towards this goal were put forward. One is known as the "tunneling from nothing" proposal by Vilenkin [1–3], which states that our universe is born through quantum tunneling from an initial quantum state with no classical geometry. The other is known as the "no boundary" proposal by Hartle and Hawking [4], which states that the wave function of our universe should be given by path integral over Euclidean geometries without a boundary corresponding to the initial time. Vilenkin's proposal can also be stated in the path integral formalism [2], in which one integrates over Lorentzian geometries unlike Hartle-Hawking's proposal. Despite their conceptual similarities, the two proposals lead to quite different consequences. For instance, the wave functions obtained by the Vilenkin and Hartle-Hawking proposals behave as $e^{-12\pi^2/\ell_{\rm P}^2\Lambda}$ and $e^{12\pi^2/\ell_{\rm P}^2\Lambda}$, respectively, where Λ is the cosmological constant and $\ell_{\rm P}$ is the Planck length. This makes a big difference when the cosmological constant is replaced by the potential of a dynamical field as in the inflation models. See refs. [5, 6] for recent reviews on these proposals and related issues.

The relationship between the two proposals can be most clearly seen [7] in the mini-superspace model, which is obtained from the Einstein-Hilbert action by assuming that the geometry to be integrated over is homogeneous and isotropic. After integrating out the scale factor while fixing the time-reparametrization invariance by requiring the lapse function to be time-independent, one is left with the integration over the lapse N. The saddle points on the complex N plane that correspond to Vilenkin and Hartle-Hawking were identified, and they actually correspond to different orientations of the Wick rotation; namely the usual one $t = -i\tau$ for the Hartle-Hawking saddle and the opposite one $t = i\tau$ for the Vilenkin saddle. Possible choice of the steepest descent contours that go through either the Vilenkin or the Hartle-Hawking saddle was also discussed, but there was no principle to choose a unique contour at that time.

Recently there has been major progress in defining the path integral for quantum gravity based on the Picard-Lefschetz theory, which provides a general prescription for rendering an oscillating integral into a sum over convergent integrals on the Lefschetz thimbles associated with relevant saddle points. Using this theory, the real-time path integral can be made totally well defined without making a Wick rotation into the imaginary time formalism. In particular, this has a big impact on the formulation of quantum gravity since the Euclidean quantum gravity is known to be pathological due to the unboundedness of the Einstein action as is manifested by the conformal mode instability [8]. Such pathology is absent in Lorentzian quantum gravity since the unboundedness simply implies increasingly violent phase rotations of the integrand, which can be dealt with by the Picard-Lefschetz theory. Therefore, a natural definition of the path integral for quantum gravity can be given by integrating over the Lorentzian geometry as advocated in ref. [9]. In particular, this fixes the ambiguity[1] in choosing the integration contour in quantum cosmology completely.[2]

In fact, the steepest descent contour specified in this way passes through the Vilenkin saddle when the Dirichlet boundary condition is imposed at the initial time. However, it has been argued that the Vilenkin saddle suffers from the instability problem if one incorporates the tensor modes and matter fields because of the "wrong" Wick rotation mentioned above [17, 18]. (See also refs. [19–24].) Based on these observations, it has been proposed [25, 26] to use the Robin boundary condition[3] at the initial time, which interpolates the Dirichlet and Neumann conditions while making the scale factor vanish on the average at the initial time. In that case, the relevant saddle point has been shown to switch from Vilenkin to Hartle-Hawking as the interpolating parameter of the Robin boundary condition is changed. Thus the no-boundary proposal with the Hartle-Hawking saddle point was realized, for the first time, within Lorentzian quantum gravity.

In this paper, we perform Monte Carlo calculations in quantum cosmology. In order to overcome the sign problem that occurs for an oscillating integral, we apply the generalized

[1] In this paper, we are primarily concerned with the propagator (i.e., Green's function), which is relevant for dynamical (Lorentzian) processes. However, in the context of using the path integral for the purpose of constructing the wave function as a solution to the Wheeler-DeWitt equation, there is no reason to prefer a Lorentzian contour. Hence, the ambiguity still remains in that context [10–12].

[2] Recently there are interesting observations related to this issue from the viewpoint of the dS_3/CFT_2 correspondence [13–16].

[3] Historically, the Robin boundary condition was introduced in quantum cosmology earlier [19, 20] in order to solve the instability problem of the Vilenkin saddle point.

JHEP05(2025)142

Lefschetz thimble method (GTM) [27], which ameliorates the sign problem by deforming the integration contour similarly to the Picard-Lefschetz theory.[4] A first step in that direction has been taken recently[5] using a simple Metropolis algorithm on the real axis [34]. Here we use a far more efficient Hybrid Monte Carlo algorithm on the deformed contour [35], which is crucial, in particular, in investigating interesting behaviors that appear in the case of Robin boundary condition. We also use the preconditioned flow equation [36] to overcome some technical problem that occurs when the number of time steps is increased. This technique has been used recently in establishing a new picture of quantum tunneling based on the real-time path integral formalism [37].

The primary aim of this work is to establish a calculation method for quantum cosmology that enables us to perform fully nonperturbative calculations that goes beyond the saddle-point approximation. Furthermore, while we restrict ourselves to the mini-superspace model in this work, the established method is flexible enough to add matter fields and/or to enlarge the mini-superspace by expanding fields in spherical harmonics and keeping a finite number of them, which is important in investigating the possible instability problem with the Vilenkin saddle mentioned above.

In particular, our numerical calculations confirm that the Vilenkin saddles become relevant in the case of Dirichlet boundary condition. The emergence of the real time is described by the Stokes phenomenon of the saddle points, which occurs as we increase the scale factor at the final time. In the case of Robin boundary condition, the relevant saddle point switches from Vilenkin to Hartle-Hawking as the interpolating parameter of the Robin boundary condition is changed. These results are obtained in a regime in which perturbation theory around saddle points breaks down as we show by explicit calculations.

We also clarify some fundamental issues in quantum cosmology, which have not been fully discussed in the literature. In particular, we discuss some issues concerning the integration domain of the lapse function. In fact, the whole real axis has to be chosen in order to obtain solutions to the Wheeler-DeWitt equation, whereas the positive real axis has to be chosen in order to calculate the Green functions of the Wheeler-DeWitt operator [38–40]. (See ref. [41] for a recent discussion.) In the case of Robin boundary condition, however, it turns out that there is a problem in choosing the positive real axis. This is due to the fact that the origin $N = 0$ is mapped to a different point by the contour deformation unlike in the case of Dirichlet boundary condition. Because of this, one obtains an unwanted contribution from the arc that starts at the origin $N = 0$ when one deforms the integration contour using Cauchy's theorem. We determine the parameter regime in which this contribution dominates over the contribution from the relevant saddle.

The rest of this paper is organized as follows. In section 2, we briefly review quantum cosmology based on the mini-superspace model with the Dirichlet and Robin boundary conditions. In section 3, we discuss the issue of the arc contribution that appears in the case of Robin boundary condition. In section 4, we explain how we deal with this model by Monte Carlo calculations using the GTM. In section 5, we present our results obtained

[4]The idea to perform Monte Carlo simulations on the Lefschetz thimble was put forward in refs. [28–31].

[5]This paper addressed the issue of the integration domain of the scale factor squared $q(t) = a^2(t)$, which is taken to be the whole real axis in analytic calculations such as the one in ref. [7]. For other numerical approaches to quantum gravity, see refs. [32, 33], for instance.

JHEP05(2025)142

by the Monte Carlo calculations. In section 6, we discuss how one can read off the real geometry from the complex geometry obtained at the saddle point. Section 7 is devoted to a summary and discussions. In appendix A, we explain the details of our calculation method. In appendix B, we derive the effective action for the lapse function in the theory with discrete time, which is used in perturbative calculations.

2 Brief review of quantum cosmology

In this section, we briefly review quantum cosmology based on the mini-superspace model, in which the space-time is assumed to be homogeneous and isotropic. Here we also assume that it has positive curvature. Then the metric can be parametrized as

$$ds^2 = a^2(\eta)(-N(\eta)^2 d\eta^2 + d\Omega_3{}^2)\,, \tag{2.1}$$

where we have defined the conformal time η, the scale factor $a(\eta)$, the lapse function $N(\eta) > 0$ and the metric $d\Omega_3{}^2$ on a unit 3-sphere. Plugging this metric into the Einstein-Hilbert action with the Gibbons-Hawking-York boundary term, we obtain[6]

$$S_{\rm EH}[a, N] = 6\pi^2 \int d\eta \left\{ -\frac{1}{N^2} a\dot{a}^2 + N(a^2 - H^2 a^4) \right\}\,,$$

where H^2 represents the cosmological constant $\Lambda \equiv 3H^2$ using the notation in refs. [25, 26].

In order to solve this model analytically, we make a change of variables [7]

$$\begin{aligned} q(t) &= a^2(\eta)\,, \\ dt &= a^2(\eta)\, d\eta\,, \end{aligned} \tag{2.2}$$

which brings the action into a quadratic form

$$S_{\rm EH}[q, N] = 6\pi^2 \int dt \left\{ -\frac{1}{4N} \dot{q}^2 + N(1 - H^2 q) \right\} \tag{2.3}$$

with respect to q, where we have introduced $\dot{q} = \frac{dq}{dt}$ and $\ddot{q} = \frac{d^2 q}{dt^2}$. In terms of the new variables, the metric (2.1) reads

$$ds^2 = -\frac{N(t)^2}{q(t)} dt^2 + q(t)\, d\Omega_3{}^2\,. \tag{2.4}$$

Following ref. [7], we quantize this theory by the path integral in terms of the canonical variables including the conjugate momenta $p(t)$ and $\pi(t)$ for $q(t)$ and $N(t)$, respectively. After fixing the time-reparametrization invariance by using the constant-lapse gauge $\dot{N} = 0$ and integrating out the associated Batalin-Fradkin-Vilkovisky ghosts as well as $\pi(t)$, we arrive at the partition function

$$Z = \int dN\, \mathcal{D}q\, \mathcal{D}p\, e^{iS}\,, \tag{2.5}$$

$$S[q, p, N] = \int dt \left[\dot{q}p + N \left\{ \frac{1}{6\pi^2} p^2 + 6\pi^2 (1 - H^2 q) \right\} \right]\,. \tag{2.6}$$

[6] Throughout this paper, we set $\hbar = c = 8\pi G_{\rm N} = 1$, which corresponds to setting the Planck length to $l_{\rm P} = \sqrt{\frac{\hbar G_{\rm N}}{c^3}} = \frac{1}{\sqrt{8\pi}}$.

JHEP05(2025)142

Here we note that H^2 that appears in (2.6) can be pulled out of the action as

$$\tilde{Z} = \int d\tilde{N}\, \mathcal{D}\tilde{q}\, \mathcal{D}p\, e^{i\tilde{S}/H^2}\,, \tag{2.7}$$

$$\tilde{S}[\tilde{q}, p, \tilde{N}] = \int dt \left[\dot{\tilde{q}}p + \tilde{N}\left\{\frac{1}{6\pi^2}p^2 + 6\pi^2(1-\tilde{q})\right\}\right]\,, \tag{2.8}$$

by rescaling $\tilde{q}(t) = H^2 q(t)$, $\tilde{N} = H^2 N$. Thus we find that H^2 plays the role of $\hbar$ in quantum mechanics, which controls the strength of quantum effects. In this section, we consider the $H^2 \to 0$ limit with fixed $\tilde{q}(t) = H^2 q(t)$, $\tilde{N} = H^2 N$, which enables us to solve the theory (2.7) by the saddle-point analysis. Remembering that we deal with the rescaled variables $\tilde{q}$ and $\tilde{N}$ from now on, we omit the tildes to simplify the notation.

2.1 Dirichlet boundary condition

Integrating out $p(t)$ in (2.7), we obtain the effective action for $q(t)$ and N as

$$S_{\text{eff}}[q, N] = 6\pi^2 \int dt\, \left\{-\frac{1}{4N}\dot{q}^2 + N(1-q)\right\}\,. \tag{2.9}$$

Taking the variation of (2.9) with respect to $q(t)$, we get

$$\delta S_{\text{eff}} = 6\pi^2 \left[\int_0^1 dt \left(\frac{1}{2N}\ddot{q} - N\right)\delta q(t) - \frac{1}{2N}\Big\{\dot{q}(1)\delta q(1) - \dot{q}(0)\delta q(0)\Big\}\right]\,, \tag{2.10}$$

from which one obtains the classical equation of motion for $q(t)$ as

$$\ddot{q} = 2N^2 \tag{2.11}$$

and the requirement for the boundary conditions

$$\dot{q}(1)\delta q(1) - \dot{q}(0)\delta q(0) = 0\,. \tag{2.12}$$

Here we impose the Dirichlet boundary conditions

$$q(0) = q_{\text{i}}\,, \qquad q(1) = q_{\text{f}} \tag{2.13}$$

on both ends, which satisfy (2.12). Solving the classical equation of motion for $q(t)$ in (2.11) with the boundary conditions (2.13), we obtain

$$\bar{q}(t) = N^2 t^2 + (-N^2 + q_{\text{f}} - q_{\text{i}})\, t + q_{\text{i}}\,. \tag{2.14}$$

The effective action for N after integrating out $q(t)$ can be obtained in the $H^2 \to 0$ limit by just substituting the classical solution $q(t) = \bar{q}(t)$ in the action (2.9) as[7]

$$S_{\text{eff}}(N) = \pi^2 \left\{\frac{N^3}{2} - 3N(q_{\text{f}} + q_{\text{i}} - 2) - \frac{3}{2N}(q_{\text{f}} - q_{\text{i}})^2\right\}\,. \tag{2.15}$$

[7]Note that the N-dependent factors arising from integrating out $p(t)$ and $q(t)$ need not be included in the effective action (2.9) and (2.15) in the $H^2 \to 0$ limit considered here although it should be taken into account in the full quantum calculations as we discuss in section 4.

JHEP05(2025)142

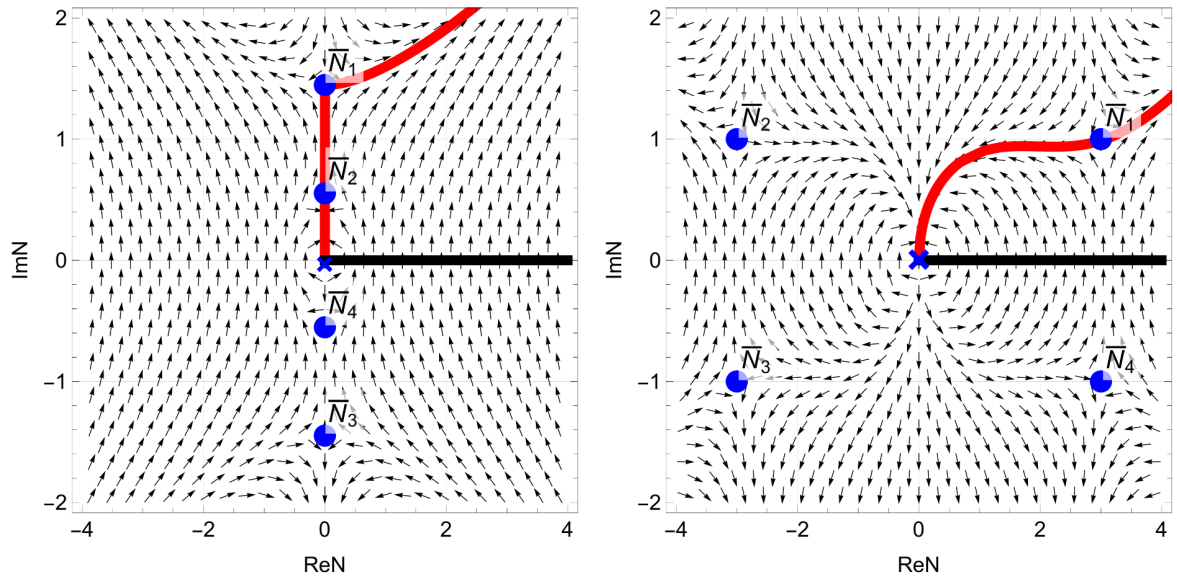

Figure 1. The flow diagram is shown in the case of Dirichlet boundary conditions $q_{\rm i} = 0$ at $t = 0$ and $q_{\rm f} = 0.8$ (Left), 10 (Right) at $t = 1$, respectively. Blue circles represent the saddle points $\bar{N}_1$, $\bar{N}_2$, $\bar{N}_3$, $\bar{N}_4$, which correspond to $(c_1, c_2) = (1, 1)$, $(-1, 1)$, $(-1, -1)$, $(1, -1)$ in (2.18), respectively. The blue crosses represent the singularities of the effective action. The black line represents the original integration contour, while the red line represents the integration contour obtained by the Picard-Lefschetz theory.

Taking the derivative of (2.15) with respect to N, we obtain the saddle-point equation

$$N^4 - 2(q_{\rm f} + q_{\rm i} - 2)N^2 + (q_{\rm f} - q_{\rm i})^2 = 0\,, \tag{2.16}$$

which can be factorized as

$$\left\{N^2 - 2\sqrt{q_{\rm i} - 1}N - (q_{\rm f} - q_{\rm i})\right\}\left\{N^2 + 2\sqrt{q_{\rm i} - 1}N - (q_{\rm f} - q_{\rm i})\right\} = 0\,. \tag{2.17}$$

Thus we obtain four solutions[8]

$$\bar{N} = c_1\sqrt{q_{\rm f} - 1} + c_2\sqrt{q_{\rm i} - 1}\,, \tag{2.18}$$

where c_1, $c_2 \in \{1, -1\}$. Let us label them as $\bar{N}_1$, $\bar{N}_2$, $\bar{N}_3$, $\bar{N}_4$ corresponding to $(c_1, c_2) = (1, 1)$, $(-1, 1)$, $(-1, -1)$, $(1, -1)$, respectively.

In what follows, we set $q_{\rm i} = 0$ in order to realize the "no boundary" proposal. Then the saddle points become

$$\bar{N} = c_1\sqrt{q_{\rm f} - 1} + ic_2\,. \tag{2.19}$$

Using $\bar{N}^2 - 2ic_2\bar{N} - q_{\rm f} = 0$ in (2.14), the classical solution $\bar{q}(t)$ can be rewritten as

$$\bar{q}(t) = \bar{N}^2t^2 - 2ic_2\bar{N}t\,. \tag{2.20}$$

[8]Here we define $\sqrt{q_{\rm f} - 1} \equiv i\sqrt{1 - q_{\rm f}}$ for $q_{\rm f} < 1$ and similarly for $\sqrt{q_{\rm i} - 1}$.

JHEP05(2025)142

The integration contour for the lapse function N can be obtained by the Picard-Lefschetz theory, which amounts to deforming the original integration contour $\mathbb{R}_+$ in the complex N plane using the flow equation[9]

$$\frac{\partial N(\tau)}{\partial \tau} = i \overline{\frac{\partial S_{\rm eff}(N(\tau))}{\partial N}}\,, \tag{2.21}$$

where $N(\tau)$ represents the lapse function at the flow time τ and $S_{\rm eff}(N)$ represents the effective action (2.15). The initial condition $N(0)$ of the flow equation is given by some point on the original integration contour $\mathbb{R}_+$. The deformed integration contour obtained in the $\tau \to \infty$ limit passes through some saddle points, which are considered relevant.[10]

In figure 1, we plot the right-hand side of (2.21) as small arrows in the complex N plane. The black line and the red line represent the original integration contour and the deformed integration contour, respectively. For $q_{\rm f} < 1$ (Left), $\bar{N}_1$ and $\bar{N}_2$ are relevant with the latter being the dominant one, whereas for $q_{\rm f} > 1$ (Right), $\bar{N}_1$ is the only relevant saddle.

All these relevant saddles are considered to be of the Vilenkin type since $\mathrm{Im}\bar{N} > 0$, which corresponds to the wrong Wick rotation. (See section 6 for the details.) Thus there is a possibility of the instability problem when one goes beyond the mini-superspace model [17, 18].

2.2 Robin boundary condition

In order to make the saddle points of the Hartle-Hawking type relevant, it was proposed [25, 26] to impose the Robin boundary condition at $t = 0$ as

$$\frac{3\pi^2}{N}\dot{q}(0) + \alpha + \frac{q(0)}{\beta} = 0\,, \tag{2.22}$$

where α and β are complex parameters to be fixed later, while keeping the Dirichlet boundary condition $q(1) = q_{\rm f}$ at $t = 1$. Note that the Robin boundary condition (2.22) interpolates the Dirichlet boundary condition (with $q(0) = 0$) at $\beta = 0$ and the Neumann boundary condition (with $\dot{q}(0) = -\frac{N}{3\pi^2}\alpha$) at $\beta = \infty$.

In fact, when the Neumann boundary condition is used, it is known [7] that either Vilenkin saddles or Hartle-Hawking saddles appear in the complex N plane depending on the sign of the initial Euclidean momentum $-i\,\dot{q}(0) = i\frac{N}{3\pi^2}\alpha$. Furthermore, by choosing the value of the initial Euclidean momentum appropriately, one can make the scale factor vanish at the initial time for classical solutions. However, quantum fluctuations of the scale factor diverge due to the uncertainty relation with fixed momentum. This is the motivation for considering the Robin boundary condition.[11]

[9] This is nothing but the anti-holomorphic gradient flow equation (A.3) applied to a single variable N with the action $S(N) = -i\,S_{\rm eff}(N)$.

[10] See ref. [42] for a careful analysis in this regard from the viewpoint of the resurgence theory.

[11] In order to make the Robin boundary condition consistent with the variational principle, one needs to add a boundary term (2.23) to the action by hand. This is allowed from the viewpoint of defining Green's function, which is taken throughout this paper. Note, however, that this is not allowed from the viewpoint of defining the wave function satisfying the Wheeler-DeWitt equation based on the no-boundary proposal, which requires the space-time manifold to have no boundary to the past.

JHEP05(2025)142

In order to obtain (2.22), we add a boundary term[12] to the action (2.9) given by

$$\tilde{S}_{\rm B} = \alpha\, q(0) + \frac{q(0)^2}{2\beta}\,. \tag{2.23}$$

Taking the variation of (2.23) and combining it with (2.10), we obtain

$$-\frac{3\pi^2}{N}\dot{q}(1)\delta q(1) + \left(\frac{3\pi^2}{N}\dot{q}(0) + \alpha + \frac{q(0)}{\beta}\right)\delta q(0) = 0\,, \tag{2.24}$$

which imposes (2.22) on the classical solution since $q(0)$ is not fixed.

Similarly to the Dirichlet case, we first solve the classical equation of motion in (2.11) with the boundary conditions (2.22) and $q(1) = q_{\rm f}$ as

$$\bar{q}(t) = N^2t^2 - \frac{\alpha\beta + q_{\rm f} - N^2}{3\pi^2\beta - N}Nt + \frac{3\pi^2(q_{\rm f} - N^2) + N\alpha}{3\pi^2\beta - N}\beta\,, \tag{2.25}$$

and obtain the effective action

$$S_{\rm eff}(N) = \frac{\pi^2\left\{N^4 - 6N^2(q_f - 2) - 3q_f^2\right\} - \beta\left\{6\pi^2\alpha\left(q_f - N^2\right) + 12\pi^4 N\left(N^2 - 3q_f + 3\right) + \alpha^2 N\right\}}{2\left(N - 3\pi^2\beta\right)}\,. \tag{2.26}$$

It turns out that (2.26) can be rewritten as

$$S_{\rm eff}(N) = \pi^2\left\{\frac{X^3}{2} - 3X(q_{\rm f} + A - 2) - \frac{3}{2X}(q_{\rm f} - A)^2\right\} + \text{const.}\,, \tag{2.27}$$

where we have defined $X \equiv N - 3\pi^2\beta$ and $A \equiv 9\pi^4\beta^2 - \alpha\beta$. Since this has the same form as (2.15) up to the irrelevant constant term with the correspondence $X \leftrightarrow N$ and $A \leftrightarrow q_{\rm i}$, we can readily obtain four saddle points as

$$\bar{N} = c_1\sqrt{q_{\rm f} - 1} + c_2\sqrt{9\pi^4\beta^2 - \alpha\beta - 1} + 3\pi^2\beta\,, \tag{2.28}$$

where $c_1, c_2 \in \{1, -1\}$. Note that these saddle points reduce to those of the Dirichlet boundary conditions (2.18) with $q_{\rm i} = 0$ for $\beta = 0$. Here we define $\sqrt{9\pi^4\beta^2 - \alpha\beta - 1}$ by analytic continuation with respect to β. As in the Dirichlet case, let us label them as $\bar{N}_1$, $\bar{N}_2$, $\bar{N}_3$, $\bar{N}_4$ corresponding to $(c_1, c_2) = (1, 1)$, $(-1, 1)$, $(-1, -1)$, $(1, -1)$, respectively.

In order to realize the "no boundary" proposal, we set $\alpha = -6\pi^2 i$ from now on for the reason which will be clear shortly.[13] Plugging $\alpha = -6\pi^2 i$ in (2.28), we get

$$\bar{N} = c_1\sqrt{q_{\rm f} - 1} + c_2(i + 3\pi^2\beta) + 3\pi^2\beta\,, \tag{2.29}$$

[12] This boundary term cannot be derived from a covariant term. See ref. [26] for an alternative boundary condition, which is compatible with a covariant boundary term. See also refs. [43, 44] for applications of the Robin boundary condition to the Gauss-Bonnet gravity.

[13] Similarly, if one chooses the opposite sign $\alpha = 6\pi^2 i$, one finds that the four saddle points become $\bar{N}_{1,2} = i \pm \sqrt{q_{\rm f} - 1}$ and $\bar{N}_{3,4} = -i \mp \sqrt{q_{\rm f} - 1} + 6\pi^2\beta$. Thus the saddle points $\bar{N}_{1,2}$ are the same as in the Dirichlet case, and in particular, they satisfy $\bar{N}^2 - 2i\bar{N} - q_{\rm f} = 0$. Using this in (2.25) with $\alpha = 6\pi^2 i$, we obtain $\bar{q}(t) = \bar{N}^2t^2 - 2i\bar{N}t$, which is the same as (2.20) with $c_2 = 1$. Thus, with this choice $\alpha = 6\pi^2 i$, we can make $\bar{q}(0) = 0$ for $\bar{N}_1$ and $\bar{N}_2$ for arbitrary β. For the saddle points $\bar{N}_3$ and $\bar{N}_4$, one obtains $\bar{q}(t) = \bar{N}^2t^2 + 2(i + 6\pi^2\beta)\bar{N}t + 12\pi^2\beta(-i + 3\pi^2\beta)$, which do not satisfy $\bar{q}(0) = 0$ except for $\beta = 0, \frac{i}{3\pi^2}$.

JHEP05(2025)142

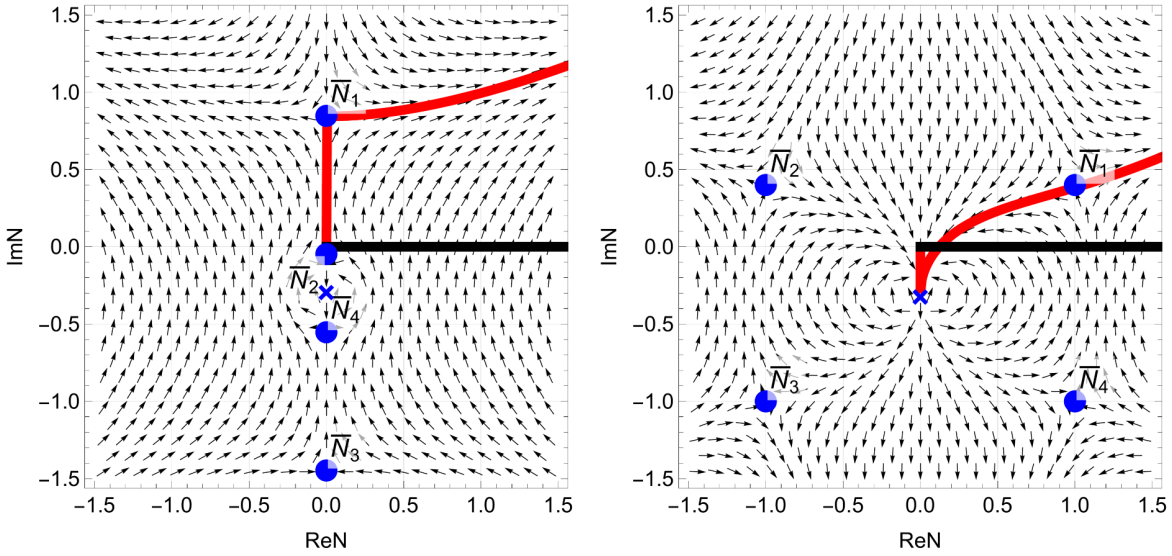

Figure 2. The flow diagram is shown similarly to figure 1 in the case of Robin boundary condition (2.22) at $t = 0$ with $\alpha = -6\pi^2 i$ and $\beta = -0.3i\tilde{\beta}_{\rm c}$, while imposing the Dirichlet boundary condition $q_{\rm f} = 0.8$ (Left) and $q_{\rm f} = 10$ (Right), respectively, at $t = 1$.

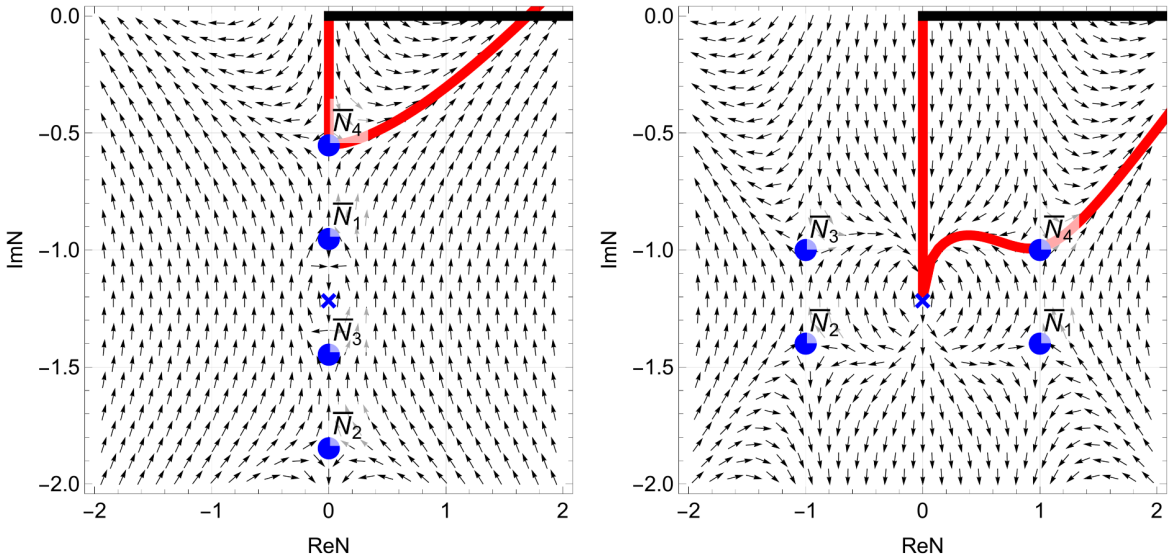

Figure 3. The flow diagram is shown similarly to figure 1 in the case of Robin boundary condition (2.22) at $t = 0$ with $\alpha = -6\pi^2 i$ and $\beta = -1.2i\tilde{\beta}_{\rm c}$, while imposing the Dirichlet boundary condition $q_{\rm f} = 0.8$ (Left) and $q_{\rm f} = 10$ (Right), respectively, at $t = 1$.

JHEP05(2025)142

which implies that

$$\bar{N}_{1,2} = i \pm \sqrt{q_{\rm f} - 1} + 6\pi^2\beta\,, \tag{2.30}$$

$$\bar{N}_{3,4} = -i \mp \sqrt{q_{\rm f} - 1}\,. \tag{2.31}$$

Thus the saddle points $\bar{N}_{3,4}$ are the same as in the Dirichlet case, and in particular, they satisfy $\bar{N}^2 + 2i\bar{N} - q_{\rm f} = 0$. Using this in (2.25) with $\alpha = -6\pi^2 i$, we obtain

$$\bar{q}(t) = \bar{N}^2 t^2 + 2i\bar{N}t\,, \tag{2.32}$$

which is the same as (2.20) with $c_2 = -1$. Thus, with this choice $\alpha = -6\pi^2 i$, we can make $\bar{q}(0) = 0$ for $\bar{N}_{3,4}$ for arbitrary β [25, 26]. Similarly, for the saddle points $\bar{N}_{1,2}$, we obtain

$$\bar{q}(t) = \bar{N}^2 t^2 - 2(i + 6\pi^2\beta)\bar{N}t + 12\pi^2\beta(i + 3\pi^2\beta)\,, \tag{2.33}$$

which do not satisfy $\bar{q}(0) = 0$ except for $\beta = 0,\ -\frac{i}{3\pi^2}$.

Below we focus on $\beta = -i\tilde{\beta}$ with $\tilde{\beta} \in \mathbb{R}_+$, which shifts the saddle points $\bar{N}_1$ and $\bar{N}_2$ downwards in the complex N plane as we increase $\tilde{\beta}$ while $\bar{N}_3$ and $\bar{N}_4$ remain the same, as one can see from (2.30) and (2.31). Note, in particular, that $\bar{N}_1$ and $\bar{N}_2$ go below $\bar{N}_4$ and $\bar{N}_3$, respectively, in the complex plane at the critical value $\tilde{\beta}_{\rm c} \equiv \frac{1}{3\pi^2}$.

Let us first discuss the case $\tilde{\beta} < \tilde{\beta}_{\rm c}$. In figure 2, we show the flow diagram for the application of the Picard-Lefschetz theory to (2.26). For both $q_{\rm f} = 0.8$ (Left) and $q_{\rm f} = 10$ (Right), the relevant saddle point is $\bar{N}_1$, which is of the Vilenkin type.[14]

Next we consider the case $\tilde{\beta} > \tilde{\beta}_{\rm c}$. The flow diagram is shown in figure 3. For both $q_{\rm f} < 1$ (Left) and $q_{\rm f} > 1$ (Right), the relevant saddle point is $\bar{N}_4$, which is of the Hartle-Hawking type, and the corresponding scale factor satisfies $\bar{q}(0) = 0$ due to the chosen $\alpha = -6\pi^2 i$.

Thus the use of Robin boundary condition has enabled the realization of the no-boundary proposal with the Hartle-Hawking saddle points for the first time [25, 26] within Lorentzian quantum gravity. However, there is an issue when one deforms the contour since the end point $N = 0$ of the integration region flows to another point, say $N = N^{(0)}$, unlike the case of Dirichlet boundary condition, where the end point $N = 0$ coincides with the singularity and hence does not flow. (See figure 1.) This implies that the integration over the "arc" between $N = 0$ and $N = N^{(0)}$ has to be taken into account in the path integral when one applies Cauchy's theorem.

3 The arc problem for Robin boundary condition

In this section, we discuss the issue concerning the arc contribution that appears in the case of Robin boundary condition. In particular, we determine the region of $q_{\rm f}$ in which the arc contribution dominates over the contribution from the thimble going through the relevant saddle point in the $H^2 \to 0$ limit.

Let us note that the effective action (2.26) appears in the partition function as $Z = \int dN e^{iS_{\rm eff}/H^2}$. Since the relative weight $Z(N) \equiv |e^{iS_{\rm eff}(N)/H^2}|$ for each N decreases along the

[14] As we discuss in section 3, for $\tilde{\beta} \leq \tilde{\beta}_{\rm c}/2$, there is a region $q_{\rm c}(\tilde{\beta}) \leq q_{\rm f} \leq 1$ in which the relevant saddle points are $\bar{N}_1$ and $\bar{N}_2$.

JHEP05(2025)142

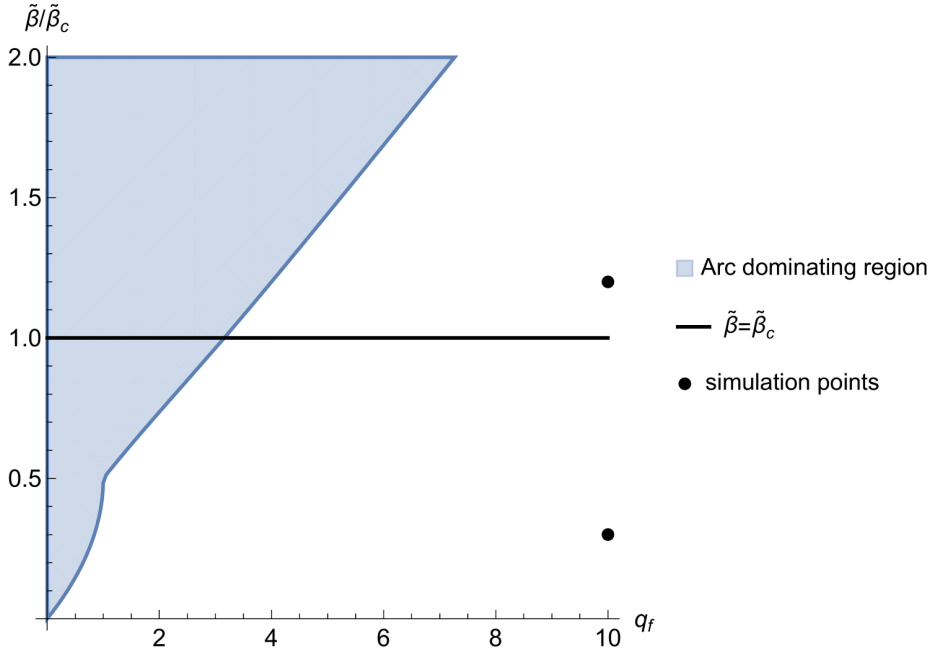

Figure 4. The shaded region represents the region of $q_{\rm f}$ and $\tilde{\beta}$ in which the arc contribution that appears in the case of Robin boundary condition dominates over the contribution from the thimble going through the relevant saddle point. The dots represent the parameter sets used for our simulations in section 5, which correspond to figure 2 (Right) and figure 3 (Right), respectively.

flow from $N = 0$, the integral along the arc can be evaluated by the value at $N = 0$ as

$$Z(0) = \exp\left\{-\frac{q_{\rm f}(q_{\rm f} - 12\pi^2\tilde{\beta})}{2\tilde{\beta}H^2} + O(1)\right\} \tag{3.1}$$

in the $H^2 \to 0$ limit. On the other hand, substituting $N = 0$ in the classical solution (2.25), one obtains $\bar{q}(t) = q_{\rm f}$, which implies that there is no time-evolution. Thus the dominance of the arc contribution poses a serious problem in quantum cosmology.

Let us first consider the case $\tilde{\beta} > \tilde{\beta}_{\rm c}$. The relevant saddle point is $\bar{N}_4$. Plugging (2.31) in the effective action (2.26), we obtain

$$Z(\bar{N}_4) = \begin{cases} \exp\left\{\frac{4\pi^2}{H^2} + O(1)\right\} & \text{for } q_{\rm f} > 1\,, \\ \exp\left\{\frac{4\pi^2}{H^2}\left(1 - (1-q_{\rm f})^{3/2}\right) + O(1)\right\} & \text{for } q_{\rm f} < 1\,. \end{cases} \tag{3.2}$$

The condition for the dominance of the arc contribution is given by $Z(0) > Z(\bar{N}_4)$. For $q_{\rm f} > 1$, we obtain

$$q_{\rm f} < q_{\rm c}(\tilde{\beta}) \equiv 6\pi^2\tilde{\beta} + 2\pi\sqrt{\tilde{\beta}(9\pi^2\tilde{\beta} - 2)}\,. \tag{3.3}$$

Note that $q_{\rm c}(\tilde{\beta}) > q_{\rm c}(\tilde{\beta}_{\rm c}) = 2(1 + \frac{1}{\sqrt{3}})$ for $\tilde{\beta} > \tilde{\beta}_{\rm c}$. For $q_{\rm f} < 1$, we obtain

$$\tilde{\beta} > \frac{q_{\rm f}^2}{4\pi^2\left(-2 + 2\sqrt{1-q_{\rm f}} + 3q_{\rm f} - 2\sqrt{q_{\rm f}-1}q_{\rm f}\right)}\,. \tag{3.4}$$

JHEP05(2025)142

Since the right-hand side, which we denote as $f(q_{\rm f})$, decreases monotonically for $0 < q_{\rm f} < 1$, its maximum is given by $\lim_{q_{\rm f}\to 0} f(q_{\rm f}) = \frac{1}{3\pi^2} = \tilde{\beta}_{\rm c}$. Hence, this inequality is always satisfied. Combining these two results, we conclude that the contribution of the arc dominates for $q_{\rm f} < q_{\rm c}(\tilde{\beta})$ in the $H^2 \to 0$ limit.

Similar analysis can be done for $\tilde{\beta} < \tilde{\beta}_{\rm c}$. At the critical point $\tilde{\beta} = \tilde{\beta}_{\rm c}$, the relevant saddle point for $q_{\rm f} > 1$ switches from $\bar{N}_4$ to $\bar{N}_1$. Therefore, the condition of our interest becomes $Z(0) > Z(\bar{N}_1)$, which gives $q_{\rm f} < q_{\rm c}(\tilde{\beta}) \equiv 6\pi^2\tilde{\beta} + 2\pi\sqrt{\tilde{\beta}(2 - 27\pi^2\tilde{\beta} + 108\pi^4\tilde{\beta}^2 - 108\pi^6\tilde{\beta}^3)}$ for $\tilde{\beta} \geq \tilde{\beta}_{\rm c}/2$. At $\tilde{\beta} = \tilde{\beta}_{\rm c}/2$, one finds that the relevant saddle point $\bar{N}_1$ lies on the real axis and the above expression gives $q_{\rm c}(\tilde{\beta}_{\rm c}/2) = 1$. Therefore, one has to consider the $q_{\rm f} < 1$ region for $\tilde{\beta} < \tilde{\beta}_{\rm c}/2$. In this case, the arc contribution dominates when $\bar{N}_2$ lies on the lower half-plane as one can see from figure 2 (Left), which gives $q_{\rm f} < q_{\rm c}(\tilde{\beta}) \equiv 12\pi^2\tilde{\beta}(1 - 3\pi^2\tilde{\beta})$.

Thus we obtain figure 4, where we show the parameter region in which the arc problem occurs. For instance, in figure 2 ($\tilde{\beta} = 0.3\tilde{\beta}_{\rm c}$) and figure 3 ($\tilde{\beta} = 1.2\tilde{\beta}_{\rm c}$), the arc problem occurs on the left ($q_{\rm f} = 0.8$), but not on the right ($q_{\rm f} = 10$).

4 Applying the GTM to quantum cosmology

Since the integrand of the partition function (2.7) of quantum cosmology is a pure phase factor, it is difficult to apply ordinary Monte Carlo methods due to the sign problem. In this section, we explain how to apply the GTM, which is a promising method to overcome the sign problem. See appendix A for a brief review of the GTM.

4.1 Discretized model for the Dirichlet boundary condition

Let us first discuss how to discretize the mini-superspace model in the case of Dirichlet boundary conditions. We start from the partition function (2.7) with the Dirichlet boundary conditions $q(0) = 0$ and $q(1) = q_{\rm f}$.

We discretize the time coordinate t with the step size ϵ satisfying $n\epsilon = 1$ and define $q_k = q(k\epsilon)$, where $k = 0, \cdots, n$, and $p_k = p((k - \frac{1}{2})\epsilon)$, where $k = 1, \cdots, n$. Then the partition function can be written as[15]

$$
\begin{aligned}
Z &= \int dN \int \prod_{k=1}^{n-1} dq_k \int \prod_{k=1}^{n} dp_k \, e^{iS/H^2} \,, \\
S &= \sum_{k=1}^{n} \epsilon \left[\frac{(q_k - q_{k-1})\, p_k}{\epsilon} + \frac{N}{6\pi^2} \left\{ p_k^2 + 36\pi^4 \left(1 - \frac{q_k + q_{k-1}}{2} \right) \right\} \right] \,,
\end{aligned}
\tag{4.1}
$$

where we impose the Dirichlet boundary conditions $q_0 = 0$ and $q_n = q_{\rm f}$. Integrating out p_k, we get the effective theory for q_k and N as

$$
Z = \int dN \, N^{-n/2} \int \prod_{k=1}^{n-1} dq_k \, e^{iS_{\rm eff}/H^2} \,, \tag{4.2}
$$

$$
S_{\rm eff} = 6\pi^2\epsilon \sum_{k=1}^{n} \left\{ -\frac{1}{4N} \left(\frac{q_k - q_{k-1}}{\epsilon} \right)^2 + N \left(1 - \frac{q_k + q_{k-1}}{2} \right) \right\} \,, \tag{4.3}
$$

omitting an overall constant factor.

[15] The integration measure for q_k and p_k is taken to be shift symmetric following ref. [7], which is based on the standard canonical quantization procedure regarding q_k and p_k as the canonically conjugate variables.

JHEP05(2025)142

Taking the derivative of the effective action S_{eff} with respect to q_k, we obtain

$$\frac{1}{\epsilon}\left(\frac{q_{k+1}-q_k}{\epsilon}-\frac{q_k-q_{k-1}}{\epsilon}\right)=2N^2 \qquad \text{for } k=1,\cdots,n-1\,, \tag{4.4}$$

which becomes the classical equation of motion (2.11) for $q(t)$ in the $\epsilon\to 0$ limit correctly.

Note that $N=0$ is a singularity of the effective action (2.15) after integrating out $q(t)$, which remains to be the case also for the discretized model; see (B.3). Therefore, one cannot cross $N=0$ during the simulation[16] based on the HMC algorithm, which is used in this work. (See appendix A for the details.) Namely, if the initial value of N is chosen to be positive, it remains to be always positive. Thus the integration domain of N is practically restricted to the $N>0$ region.

4.2 Discretized model for the Robin boundary condition

As for the case of Robin boundary condition, we derive the explicit form of the partition function starting from the path integral formalism in the phase space q_k and p_k generalizing the derivation given in ref. [7] for Dirichlet and Neumann boundary conditions.

Let us consider the partition function (2.7) with the action (2.8) plus the boundary term (2.23) as

$$Z=\int dN\int\mathcal{D}q\int\mathcal{D}p\,e^{iS/H^2}\,, \tag{4.5}$$

$$S[p,q,N]=\int dt\left[\dot{q}p+\frac{N}{6\pi^2}\{p^2+36\pi^4(1-q)\}\right]+\left(\alpha q(0)+\frac{q(0)^2}{2\beta}\right), \tag{4.6}$$

where we impose the Dirichlet boundary condition $q(1)=q_{\text{f}}$ at the final time.

As we did in the previous section, we discretize the time coordinate t and obtain

$$Z=\int dN\int\prod_{k=0}^{n-1}dq_k\int\prod_{k=1}^{n}dp_k\,e^{iS/H^2}\,, \tag{4.7}$$

$$S=\sum_{k=1}^{n}\epsilon\left[\frac{(q_k-q_{k-1})\,p_k}{\epsilon}+\frac{N}{6\pi^2}\left\{p_k^2+36\pi^4\left(1-\frac{q_k+q_{k-1}}{2}\right)\right\}\right]+\left(\alpha q_0+\frac{q_0^2}{2\beta}\right), \tag{4.8}$$

where we impose the Dirichlet boundary condition $q_n=q_{\text{f}}$ at the final time. Integrating out p_k, we obtain

$$Z=\int dN\,N^{-n/2}\int\prod_{k=0}^{n-1}dq_k\,e^{iS_{\text{eff}}/H^2}\,, \tag{4.9}$$

$$S_{\text{eff}}=6\pi^2\epsilon\sum_{k=1}^{n}\left\{-\frac{1}{4N}\left(\frac{q_k-q_{k-1}}{\epsilon}\right)^2+N\left(1-\frac{q_k+q_{k-1}}{2}\right)\right\}+\left(\alpha q_0+\frac{q_0^2}{2\beta}\right), \tag{4.10}$$

omitting an overall constant factor.

[16] In the GTM, we deform the integration contour into the complex plane by solving the gradient flow (A.3). When we say that N cannot cross $N=0$, we actually mean the value of N before the flow.

JHEP05(2025)142

Taking the derivative of the effective action S_{eff} with respect to q_k $(k = 1, \cdots, n-1)$, we obtain the classical equation of motion (4.4) as before. Taking the derivative of S_{eff} with respect to q_0, we obtain

$$\frac{3\pi^2}{N}\left(\frac{q_1 - q_0}{\epsilon} - N^2\epsilon\right) + \alpha + \frac{q_0}{\beta} = 0\,. \tag{4.11}$$

Let us note here that

$$\frac{q_1 - q_0}{\epsilon} \simeq q'\left(\frac{\epsilon}{2}\right) = q'(0) + \frac{\epsilon}{2}q''(0) = q'(0) + N^2\epsilon\,. \tag{4.12}$$

Thus, in the $\epsilon \to 0$ limit, (4.11) reduces to the Robin boundary condition (2.22), which is imposed on the classical solution. As we explained in section 2.2, we set $\alpha = -6\pi^2 i$ and $\beta = -i\tilde{\beta}$ with $\tilde{\beta} \in \mathbb{R}_+$.

Let us note here that the action (4.10) is singular at $N = 0$, which causes a problem if the value of N before the flow in the GTM comes close to $N = 0$. In the case of Dirichlet boundary condition discussed in section 4.1, the point $N = 0$ is also a singularity of the effective action (2.15) (See figure 1.), and hence it is not approached during the simulation. In the case of Robin boundary condition, however, the singularity of the effective action (2.26) is shifted to $N_{\text{sing}} = -3\pi^2 i\tilde{\beta}$ (See figures 2 and 3.), and hence $N = 0$ may be approached. In fact, this problem does not occur in practice for $q_{\text{f}} > q_{\text{c}}(\tilde{\beta})$, where $q_{\text{c}}(\tilde{\beta})$ is obtained in section 3, since in that region the contribution from the arc is suppressed compared with the contribution from the thimble that goes through the relevant saddle point. Therefore the simulation is restricted practically to the $N > 0$ region before the flow, and one cannot cross $N = 0$ and go into the $N < 0$ region. The situation is similar to the case of Dirichlet boundary condition. Hence the calculation corresponds to integrating over the thimble associated with the relevant saddle with $\text{Re}\bar{N} > 0$ without including the arc contribution, which is a good approximation as far as $q_{\text{f}} \gg q_{\text{c}}(\tilde{\beta})$. We restrict ourselves to this case in our simulation.

In refs. [25, 26], it was proposed to extend the integration contour to the whole real axis so that there is no contribution from the arc in the whole parameter region. If one wishes to perform Monte Carlo simulation in this case, one needs to be able to go across the singular point $N = 0$ in the action during the simulation. This is possible by shifting the integration contour of N in the direction of the flow as $N \mapsto N + i\delta$ with some small real constant δ. In addition to this issue, for $q_{\text{f}} > q_{\text{c}}(\tilde{\beta})$, the probability of approaching the region $\text{Re}N \sim 0$ is suppressed according to the discussion in section 3. Therefore, in order to be able to sample configurations in the $\text{Re}N > 0$ and $\text{Re}N < 0$ regions with equal weight, one needs to use a more sophisticated version of the GTM that makes it possible to sample configurations from multiple thimbles [45, 46]. We leave these cases for future investigations.

5 Results of the simulations

In this section, we present the results of our simulation. In particular, we compare the cases of the Dirichlet and Robin boundary conditions at the initial time, and discuss how the relevant saddle point changes from that of the Vilenkin type to that of the Hartle-Hawking type in the case of Robin boundary condition as we change the parameter β. For all the simulations in this work, the number of steps in time is chosen to be $n = 10$. We have verified that the result does not change significantly by increasing n to 20.

JHEP05(2025)142

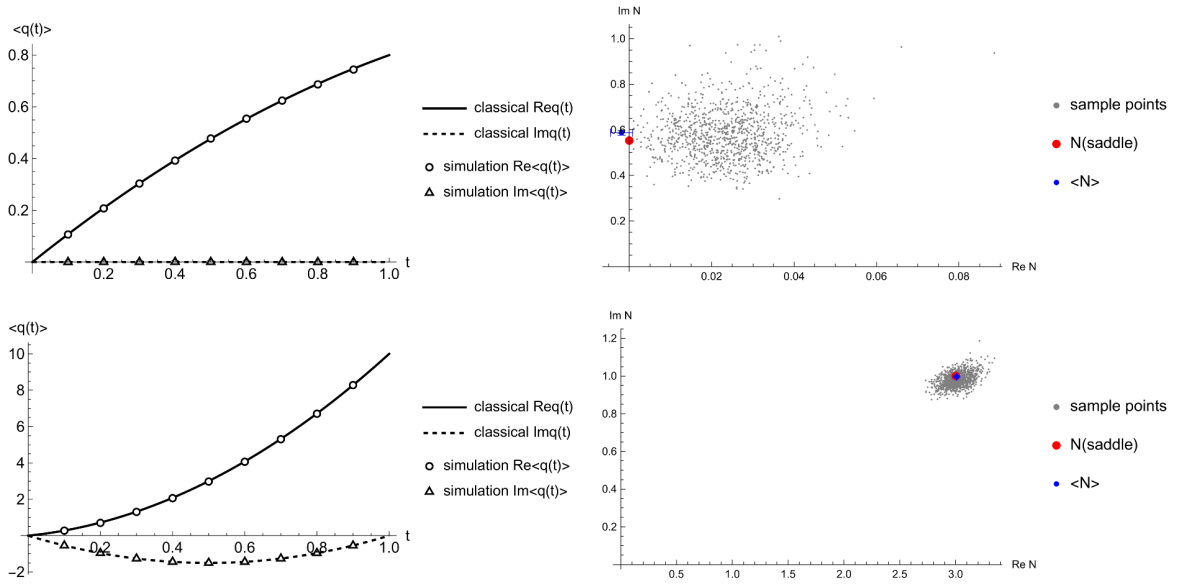

Figure 5. Simulation results are shown in the case of Dirichlet boundary condition for $H^2 = 1$ with $q_{\rm f} = 0.8$ (Top) and $q_{\rm f} = 10$ (Bottom). (Left) The expectation values $\langle q(t) \rangle$ are plotted for the real (circles) and imaginary (triangles) parts separately. The classical solutions are shown for comparison by the solid and dashed lines for the real and imaginary parts, respectively. (Right) The gray dots represent the values of N in the complex plane for each configuration obtained after the gradient flow. The blue circle represents $\langle N \rangle$, which is obtained by taking an average with a reweighting factor (A.6), whereas the red circle represents the saddle point $\bar{N}_2$ in the Top-Right panel and $\bar{N}_1$ in the Bottom-Right panel, given by (2.19) with $(c_1, c_2) = (-1, 1)$ and $(1, 1)$, respectively. The error bars for the expectation values are omitted when they are smaller than the data points.

5.1 Dirichlet boundary condition

First let us discuss the case of Dirichlet boundary condition. In figure 5 we plot the expectation values $\langle q(t) \rangle$ for $t = k\epsilon$ $(k = 1, \cdots, n-1)$ and $\langle N \rangle$ obtained for $H^2 = 1$ with $q_{\rm f} = 0.8$ (Top) and $q_{\rm f} = 10$ (Bottom), which correspond to the left and right panels of figure 1, respectively. We find good agreement with the results[17] of the saddle-point analysis (2.19) and (2.20) despite the fact that the chosen $H^2 = 1$ is not small enough to suppress quantum corrections as we discuss in section 5.3.

In particular, when $q_{\rm f} < 1$ (the upper panels), $\langle N \rangle$ is purely imaginary and $\langle q(t) \rangle$ is purely real, indicating that the geometry dominating the path integral in this case is Euclidean, and it is actually a part of a hemisphere as we discuss in section 6. The fact $\mathrm{Im}\langle N \rangle > 0$ implies that the relevant saddle is that of the Vilenkin type as expected. On the other hand, when $q_{\rm f} > 1$ (the lower panels), the real part of $\langle N \rangle$ becomes positive and $\langle q(t) \rangle$ acquires an imaginary part. Thus the dominant geometry becomes complex in this case. However, this is simply due to the chosen gauge $dN(t)/dt = 0$ for the time-reparametrization invariance, and it actually represents a part of de Sitter space capped off by a Euclidean hemisphere as we discuss in section 6. Thus the origin of real time can be identified with the Stokes

[17] Let us recall that there are two relevant saddle points in the $q_{\rm f} < 1$ case represented by $(c_1, c_2) = (\pm 1, 1)$ in (2.19). Our results agree well with the results obtained for the dominant saddle point $c_1 = -1$ as expected.

JHEP05(2025)142

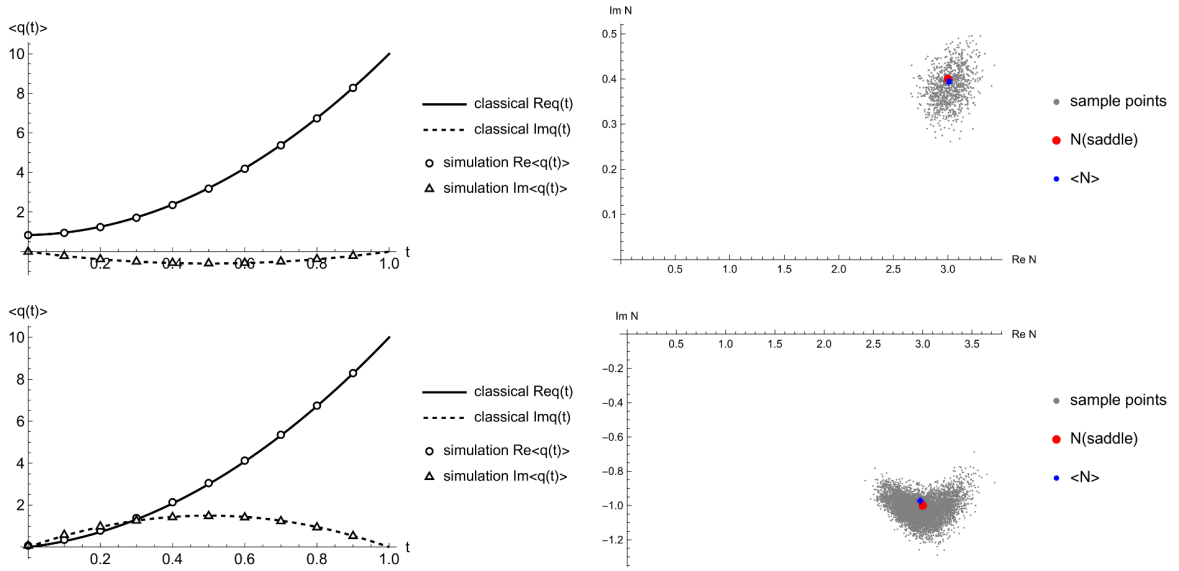

Figure 6. Similar plots to figure 5 in the case of Robin boundary condition for $H^2 = 1$ and $q_f = 10$ with $\tilde{\beta} = 0.3\tilde{\beta}_c$ (Top) and $\tilde{\beta} = 1.2\tilde{\beta}_c$ (Bottom). The red point represents $\bar{N}_1$ in the Top-Right panel and $\bar{N}_4$ in the Bottom-Right panel, given by (2.30) and (2.31), respectively.

phenomenon at the critical value $q_f = 1$ as emphasized in ref. [47]; the relevant saddle points $\bar{N}_1$ and $\bar{N}_2$ on the imaginary axis for $q_f < 1$ merge into one at $\bar{N}_1 = \bar{N}_2 = i$ for $q_f = 1$ and split into two for $q_f > 1$ acquiring the real part as we have seen in figure 1.

In the right panels, the gray dots represent the values of N calculated for sampled configurations after the gradient flow in the GTM. Note that they are not necessarily distributed around the expectation value $\langle N \rangle$, which is obtained by taking an average with a reweighting factor (A.16).

5.2 Robin boundary condition

Next we show our results in the case of Robin boundary condition. In figure 6 (Top), we plot our results for $H^2 = 1$ with $\tilde{\beta} = 0.3\tilde{\beta}_c$ and $q_f = 10$, which corresponds to figure 2 (Right). We find good agreement with the results obtained by the saddle-point analysis (2.30) and (2.33). The results are similar to the corresponding results for the Dirichlet boundary condition shown in the lower panel of figure 5 as expected. In particular, $\mathrm{Im}\langle N \rangle > 0$ implies that the relevant saddle is that of the Vilenkin type in this case. Note also that $\langle q(0) \rangle \neq 0$ due to our choice $\alpha = -6\pi^2 i$. (See eq. (2.33).)

In figure 6 (Bottom), we show our results for $H^2 = 1$ with $\tilde{\beta} = 1.2\tilde{\beta}_c$ and $q_f = 10$, which corresponds to figure 3 (Right). We find good agreement with the results obtained by the saddle-point analysis (2.31) and (2.32). In particular, $\mathrm{Im}\langle N \rangle < 0$ implies that the relevant saddle is that of the Hartle-Hawking type. Note also that $\langle q(0) \rangle \approx 0$, which confirms that the "no boundary" proposal is realized in the sense of expectation values due to the choice $\alpha = -6\pi^2 i$. On the other hand, the real part of $\langle N \rangle$ becomes positive and $\langle q(t) \rangle$ acquires an imaginary part. We will see in section 6 that the real geometry one can read off in this case is a part of de Sitter space capped off by a Euclidean hemisphere as in the Dirichlet case although one has to make a Wick rotation in the opposite orientation.

JHEP05(2025)142

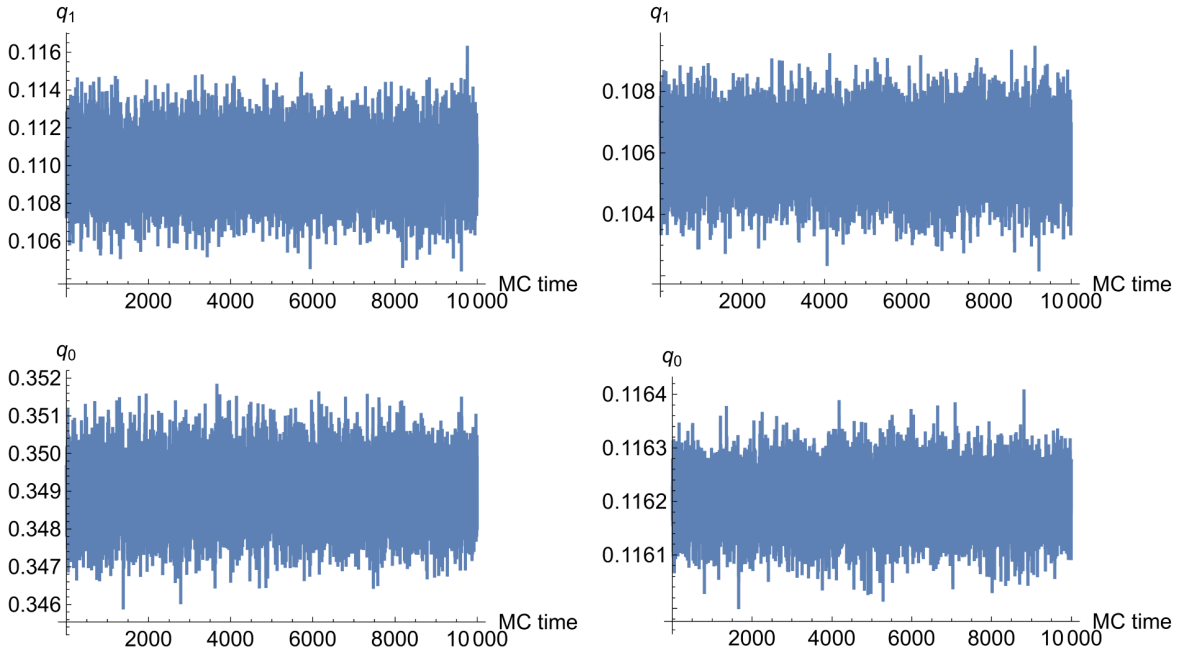

Figure 7. The Monte Carlo history of the smallest $q_k = q(k\epsilon)$ before the gradient flow in the GTM is shown. The horizontal axis refers to the number of sampled configurations. In the upper panels, we show the history of q_1 in the Dirichlet case for $H^2 = 1$ with $q_{\mathrm{f}} = 0.8$ (Left) and $q_{\mathrm{f}} = 10$ (Right). In the lower panels, we show the history of q_0 in the Robin case for $H^2 = 1$ and $q_{\mathrm{f}} = 10$ with $\tilde{\beta} = 0.3\tilde{\beta}_{\mathrm{c}}$ (Left) and $\tilde{\beta} = 1.2\tilde{\beta}_{\mathrm{c}}$ (Right).

In passing, let us also comment on the issue raised in ref. [34] concerning the change of variables (2.2). In order for the variable $q(t)$ to correspond to the scale factor squared, it is necessary that the path integral over $q(t)$ is restricted to the $q(t) \geq 0$ region. In figure 7, we present the history of the smallest $q_k = q(k\epsilon)$ [$k = 1$ for the Dirichlet case and $k = 0$ for the Robin case] before the gradient flow in the GTM. We find that only positive q_k appears during the simulation despite the fact that $\langle q_k \rangle$ is close to zero when the no-boundary proposal is realized. Thus the results obtained by our simulation correspond practically to restricting the path integral to the $q(t) \geq 0$ region.[18]

5.3 Comparison with the perturbative expansion in H^2

In all the simulation results obtained above with $H^2 = 1$, the expectation values turned out to be close to the results of the saddle-point analysis. In this section, we calculate the quantum corrections to the saddle-point results by the perturbative expansion with respect to H^2 and demonstrate that the perturbation theory breaks down at $H^2 \sim 0.1$. This implies that the simulation point $H^2 = 1$ actually lies in the nonperturbative regime, where perturbation theory is not applicable. We also perform additional simulations with $H^2 = 0.3$, 0.1, 0.03

[18] Even if this turns out not to be the case, for instance in the case of large H^2, we can make a change of variables $q(t) = e^{\sigma(t)}$ with $\sigma(t) \in \mathbb{R}$ and adopt a shift-invariant measure for $\sigma(t)$, which would exclude the $q(t) < 0$ region completely. Exploring such a model, which is inequivalent to the original one, is left for future investigations.

JHEP05(2025)142

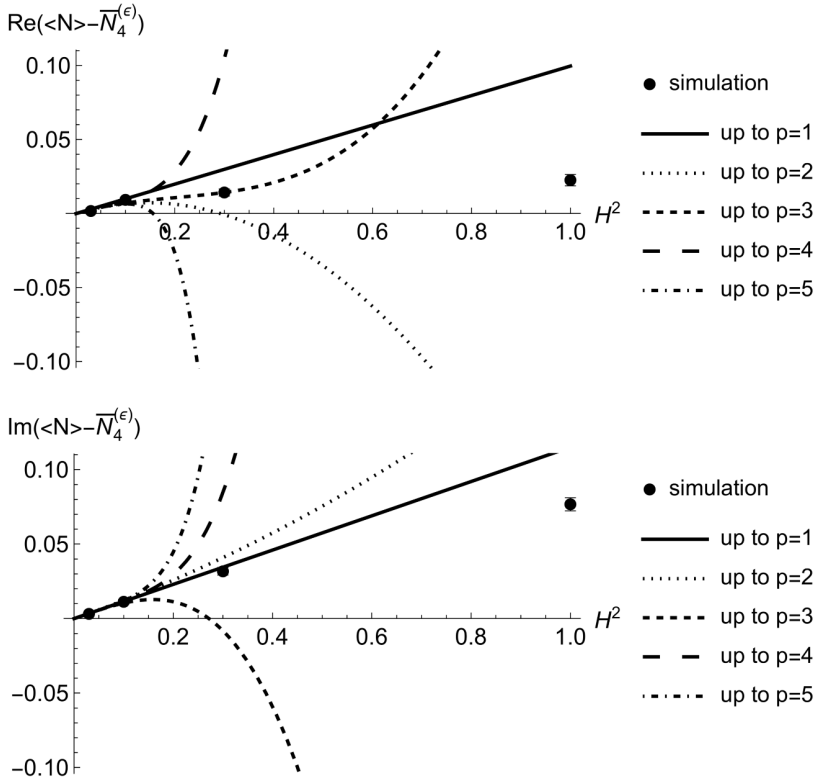

Figure 8. The expectation value $\langle N \rangle$ is plotted against H^2 for the real part (Left) and the imaginary part (Right), respectively, in the case of Robin boundary condition for various $H^2 = 0.03,\ 0.1,\ 0.3,\ 1$ with $\tilde{\beta} = 1.2\tilde{\beta}_c$ and $q_f = 10$. The lines represent the results (5.6) obtained by perturbation theory up to the p-th order ($p = 1, \cdots, 5$) in H^2 with $\epsilon = 0.1$.

in order to see the consistency with the perturbation theory. Here we focus on the case of Robin boundary condition with $\tilde{\beta} = 1.2\tilde{\beta}_c$ and $q_f = 10$.

Since our simulation uses $\epsilon = 0.1$ for discretizing the time t, we have to consider the perturbative expansion in H^2 for finite ϵ in order to make a precise comparison. For that we start from the discretized partition function (4.9). Integrating out q_k, we arrive at (See appendix B for derivation.)

$$Z = \int dN\, e^{iS_{\rm eff}[N]/H^2}\,, \tag{5.1}$$

$$S_{\rm eff}[N] = -\frac{\pi^2}{2}\left(\epsilon^2 N^3 + \frac{\beta\left(6\pi^2\alpha\left(q_f - N^2\right) + 12\pi^4 N\left(N^2 - 3q_f + 3\right) + \alpha^2 N\right)}{\pi^2\left(N - 3\pi^2\beta\right)}\right.$$
$$\left. - \frac{N^4 - 6N^2(q_f - 2) - 3q_f^2}{N - 3\pi^2\beta}\right) + \frac{i}{2}H^2 \log\left(N - 3\pi^2\beta\right)\,, \tag{5.2}$$

up to an irrelevant constant. Thus the finite ϵ effect appears only in the first term.

We obtain the solution to the saddle-point equation derived from (5.2) in the form of the H^2 expansion as

$$N^{(0)} = \bar{N}_4^{(\epsilon)} + \sum_{p=1}^{\infty} a_p\, H^{2p}\,, \tag{5.3}$$

JHEP05(2025)142

around the relevant saddle point $\bar{N}_4^{(\epsilon)}$ corresponding to $\bar{N}_4 = -i + \sqrt{q_{\rm f} - 1}$ in (2.31) in the $\epsilon \to 0$ limit. Then we substitute $N = N^{(0)} + \varphi$ in the action and calculate

$$\langle \varphi \rangle = \frac{1}{Z} \int_{-\infty}^{\infty} d\varphi \, e^{iS_{\rm eff}[N^{(0)}+\varphi]/H^2} \tag{5.4}$$

perturbatively, which yields

$$\langle N \rangle = N^{(0)} + \langle \varphi \rangle = \bar{N}_4^{(\epsilon)} + \sum_{p=1}^{\infty} \tilde{a}_p \, H^{2p} \, . \tag{5.5}$$

For $\epsilon = 0.1$ with $\tilde{\beta} = 1.2\tilde{\beta}_{\rm c}$ and $q_{\rm f} = 10$, we obtain

$$\begin{aligned} {\rm Re}\langle N \rangle &= 2.95266 + 0.099668 H^2 - 0.340375 H^4 + 0.555885 H^6 + 11.1378 H^8 - 172.735 H^{10} \, , \\ {\rm Im}\langle N \rangle &= -1.04925 + 0.115002 H^2 + 0.0718019 H^4 - 1.82104 H^6 + 11.4782 H^8 + 47.0957 H^{10} \, , \end{aligned} \tag{5.6}$$

up to the fifth order in H^2.

In figure 8, we plot the expectation value $\langle N \rangle$ for $H^2 = 0.03, 0.1, 0.3, 1$. Our results are in good agreement with the perturbative result (5.6) for $H^2 \lesssim 0.1$, which confirms the validity of our simulations. On the other hand, for $H^2 \gtrsim 0.1$, the perturbative results show diverging behaviors as the order p is increased, which implies that the perturbation theory breaks down around $H^2 \sim 0.1$. Thus $H^2 = 1$ used in our simulation for figures 5 and 6 lies in a regime in which perturbation theory is no more applicable.[19] This demonstrates the capability of our method to perform full quantum calculations in quantum cosmology.

6 Extracting real geometry from complex geometry

In this section, we discuss the metric of the space-time (2.4) for the relevant saddle points. As we have seen in sections 2.1 and 2.2, for $q_{\rm f} < 1$, $\bar{N}$ becomes purely imaginary and the metric becomes real with the Euclidean signature. On the other hand, for $q_{\rm f} > 1$, $\bar{N}$ and hence the metric becomes complex. This has something to do with the way we fix the "gauge" for the time-reparametrization invariance of the action (2.3). Here we discuss how to read off the real geometry from the complex geometry at the saddle point, refining the previous discussions on this issue. (See section III of ref. [26], for instance.)

Note first that the action (2.3) is invariant under the time-reparametrization given by

$$q(t) \mapsto \tilde{q}(t) \, , \quad N(t) \mapsto \tilde{N}(t) \, , \tag{6.1}$$

where $\tilde{q}(t)$ and $\tilde{N}(t)$ are defined by

$$\tilde{q}(f(t)) = q(t) \, , \quad \tilde{N}(f(t)) \frac{df(t)}{dt} = N(t) \, , \tag{6.2}$$

[19] The analysis in this section corresponds to our Monte Carlo results in the Bottom-Right panel of figure 6, which are obtained for the Robin boundary condition at the initial time with $H^2 = 1$, $q_{\rm f} = 10$ and $\tilde{\beta} = 1.2\tilde{\beta}_{\rm c}$. Note, however, that the red circle in figure 6 represents the saddle point for $\epsilon = 0$ unlike the saddle point $\bar{N}_4^{(\epsilon)}$ used in figure 8. The smallness of quantum corrections even in the nonperturbative regime may be attributed to the simplicity of this model, where quantum corrections are caused only by fluctuations of the lapse N. Note also that the radius of convergence for the expansion (5.6) with respect to $1/H^2$ is likely to be zero based on the ratio test, which is not surprising for perturbative expansions.

JHEP05(2025)142

for an arbitrary real function $f(t)$ with $df(t)/dt > 0$ so that $\tilde{N}(t) \geq 0$. We also require that $f(0) = 0$ and $f(1) = 1$ so that the end points remain the same. We have gauge-fixed this symmetry with the condition $dN(t)/dt = 0$, which resulted in the gauge-fixed action (2.6).

When we search for saddle points of the action (2.3), we have to complexify $q(t)$ and $N(t)$. Correspondingly, let us complexify the time-coordinate $t \mapsto \tau(t) \in \mathbb{C}$, where $\tau(0) = \tau_{\rm i}$ and $\tau(1) = \tau_{\rm f}$. This defines a contour in the complex-τ plane with the end points $\tau_{\rm i}$ and $\tau_{\rm f}$, which may be regarded as a generalization of the Wick rotation. In fact, the *value* of the action is invariant under the replacement

$$t \mapsto \tau\,, \quad q(t) \mapsto \tilde{q}(\tau)\,, \quad N(t) \mapsto \tilde{N}(\tau)\,, \tag{6.3}$$

where $\tilde{q}(\tau)$ and $\tilde{N}(\tau)$ are defined by

$$\tilde{q}(\tau(t)) = q(t)\,, \quad \tilde{N}(\tau(t))\frac{d\tau}{dt} = N(t)\,. \tag{6.4}$$

Note that this is *not* a symmetry unlike the time-reparametrization[20] since the *form* of the action is changed by deforming the integration contour $t \mapsto \tau$. In particular, one can make the lapse function $\tilde{N}(\tau) = 1$ by choosing $\tau(t)$ to be the solution to $d\tau/dt = N(t)$.

Next we point out that the value of the action in the deformed theory is invariant under the change of the τ-integration contour with the end points $\tau_{\rm i}$ and $\tau_{\rm f}$ fixed due to Cauchy's theorem as far as $q(\tau)$ and $N(\tau)$ are defined by analytic continuation. Note that this invariance is different from the invariance under (6.3) for a different choice of $\tau(t)$ with the same end points.

Finally we use the deformation (6.3) backwards to get back to the original real-time theory. Using this chain of transformations, one can transform a saddle-point configuration into an equivalent configuration, which cannot be obtained in the $dN(t)/dt = 0$ gauge. In particular, this enables us to read off the real geometry from the complex geometry at the saddle point as we see below.

Let us first discuss the case of Dirichlet boundary condition. The relevant saddle points $\bar{N}$ are given by (2.19) with $c_2 = 1$, which is of the Vilenkin type; namely $\mathrm{Im}\bar{N} > 0$, with $c_1 = \pm 1$ for $q_{\rm f} < 1$ and $c_1 = 1$ for $q_{\rm f} > 1$. The classical solution $\bar{q}(t)$ for the scale factor is given by (2.20). Below we restrict ourselves to the dominant saddle point ($c_1 = 1$) with $\mathrm{Im}\bar{N} < 1$ for $q_{\rm f} < 1$.

Let us first make a generalized Wick rotation

$$\tau = \bar{N}t\,, \tag{6.5}$$

which transforms the saddle-point configuration into

$$\bar{\tilde{q}}(\tau) = \bar{q}\left(\frac{\tau}{\bar{N}}\right) = \tau^2 - 2i\tau\,, \tag{6.6}$$

$$\bar{\tilde{N}}(\tau) = \frac{1}{\bar{N}}\,\bar{N}\left(\frac{\tau}{\bar{N}}\right) = 1\,, \tag{6.7}$$

where we have used (6.4). Thus the lapse function becomes unity.

[20] The deformed theory still has a symmetry under the time-reparametrization, which amounts to the replacement $\tau(t) \mapsto \tau(f(t))$ in (6.4).

JHEP05(2025)142

Next we change the τ-integration contour as

$$\tau(t) = \begin{cases} it & \text{for } 0 \le t \le |\mathrm{Im}\bar{N}|\,, \\ i + (t-1) & \text{for } 1 < t \le 1 + \mathrm{Re}\bar{N}\,, \end{cases} \tag{6.8}$$

which makes the classical solution $\bar{\tilde{q}}(\tau)$ real

$$\bar{\tilde{q}}(\tau(t)) = \begin{cases} -t^2 + 2t & \text{for } 0 \le t \le |\mathrm{Im}\bar{N}|\,, \\ t^2 - 2t + 2 & \text{for } 1 < t \le 1 + \mathrm{Re}\bar{N}\,, \end{cases} \tag{6.9}$$

along the new contour. For $q_{\mathrm{f}} < 1$, we have $|\mathrm{Im}\bar{N}| < 1$, $\mathrm{Re}\bar{N} = 0$ and the second lines in (6.8) and (6.9) do not exist, whereas for $q_{\mathrm{f}} > 1$, we have $|\mathrm{Im}\bar{N}| = 1$, $\mathrm{Re}\bar{N} > 0$ and the second lines exist.

Finally we use the deformation (6.3) backwards to get back to the original real-time theory. The saddle-point configuration one obtains in this way[21] is $\bar{q}(t) = \bar{\tilde{q}}(\tau(t))$, which is given by (6.9), with the lapse function given by

$$\bar{N}(t) = \begin{cases} i & \text{for } 0 \le t \le |\mathrm{Im}\bar{N}|\,, \\ 1 & \text{for } 1 < t \le 1 + \mathrm{Re}\bar{N}\,, \end{cases} \tag{6.10}$$

where we have used (6.4) again. Note that (6.10) cannot be obtained in the $dN(t)/dt = 0$ gauge. The first line in (6.10) corresponds the Euclidean regime, where the lapse function becomes purely imaginary, while the second line in (6.10), which exists for $q_{\mathrm{f}} > 1$, corresponds to the Lorentzian regime, where the lapse function becomes real. Thus we can read off the real geometry at the saddle point, which consists of the Euclidean regime at early times and the Lorentzian regime at later times.

Let us define the proper time τ_{p} by making a time-reparametrization as

$$\frac{dt}{d\tau_{\mathrm{p}}} = \sqrt{\bar{q}(t)} \tag{6.11}$$

so that the metric of the space-time (2.4) becomes

$$ds^2 = \pm d\tau_{\mathrm{p}}^2 + \bar{q}(t(\tau_{\mathrm{p}}))\, d\Omega_3{}^2\,, \tag{6.12}$$

where the symbol $\pm$ should be $(+)$ for the Euclidean regime and $(-)$ for the Lorentzian regime. By solving the differential equation (6.11), we obtain

$$t(\tau_{\mathrm{p}}) = \begin{cases} 1 - \cos\tau_{\mathrm{p}} & \text{for } 0 \le \tau_{\mathrm{p}} \le \cos^{-1}(1 - |\mathrm{Im}\bar{N}|)\,, \\ 1 + \sinh(\tau_{\mathrm{p}} - \frac{\pi}{2}) & \text{for } \frac{\pi}{2} < \tau_{\mathrm{p}} \le \frac{\pi}{2} + \sinh^{-1}(\mathrm{Re}\bar{N})\,, \end{cases} \tag{6.13}$$

which makes the classical solution $\bar{q}(t(\tau_{\mathrm{p}}))$ as

$$\bar{q}(t(\tau_{\mathrm{p}})) = \begin{cases} \sin^2\tau_{\mathrm{p}} & \text{for } 0 \le \tau_{\mathrm{p}} \le \cos^{-1}(1 - |\mathrm{Im}\bar{N}|)\,, \\ \cosh^2(\tau_{\mathrm{p}} - \frac{\pi}{2}) & \text{for } \frac{\pi}{2} < \tau_{\mathrm{p}} \le \frac{\pi}{2} + \sinh^{-1}(\mathrm{Re}\bar{N})\,. \end{cases} \tag{6.14}$$

[21] The range of time t is $t = \in [0, T]$, where $T = \mathrm{Re}\bar{N} + \mathrm{Im}\bar{N}$. In order to adjust the range to the original theory, one can rescale the time as $t \mapsto \tilde{t} = t/T$.

JHEP05(2025)142

Thus for $q_{\rm f} < 1$, the geometry of the saddle-point configuration is a part of a hemisphere, whereas for $q_{\rm f} > 1$, it becomes a part of the de Sitter space capped off by a hemisphere.

In the case of Robin boundary condition for $\tilde{\beta} > \tilde{\beta}_{\rm c}$, the relevant saddle point is given by $\bar{N}_4$ in (2.31), which is of the Hartle-Hawking type ($\mathrm{Im}\bar{N} < 0$). The classical solution $\bar{q}(t)$ for the scale factor is given by (2.32). We make a generalized Wick rotation (6.5), and change the τ-integration contour as

$$\tau = \begin{cases} -it & \text{for } 0 \le t \le |\mathrm{Im}\bar{N}|\,, \\ -i + (t-1) & \text{for } 1 < t \le 1 + \mathrm{Re}\bar{N}\,, \end{cases} \tag{6.15}$$

which makes the classical solution $\bar{\tilde{q}}(\tau)$ in the same form (6.9) as in the Dirichlet case. Thus the only difference from the case of Dirichlet boundary condition is the orientation of the Wick rotation as one can see from (6.8) and (6.15).

While we have shown clearly how to extract real geometries from the complex saddle points in the case at hand, the saddle point geometries in more general setups are inherently complex and cannot be always rendered real as described here. The complex nature of such saddle points has been explored in the recent literature, notably in ref. [48] and more specifically in refs. [49, 50] in the context of the no-boundary proposal.

7 Summary and discussions

In this paper we have discussed how to perform Monte Carlo calculations in quantum cosmology, which enable us to go beyond the previous studies based on the mini-superspace and saddle-point approximations. In particular, we have adopted the recent proposal for defining quantum gravity using the path integral over the space-time metric with the Lorentzian signature, where the oscillating integral is made well-defined by the Picard-Lefschetz theory. While the oscillating integral is difficult to deal with by standard Monte Carlo methods due to the sign problem, we overcome this problem by applying the GTM, which deforms the integration contour similarly to the Picard-Lefschetz theory. As a first step, we have applied this method to the mini-superspace model.

As for the initial condition, we have followed the no-boundary proposal, which corresponds to requiring that the scale factor should vanish at the initial time. This can be realized either by the Dirichlet or the Robin boundary condition, where in the latter case one has to generalize the no-boundary proposal to the vanishing *expectation value* of the scale factor at the initial time. In either case, the system undergoes quantum tunneling at early times, which is represented by the purely imaginary expectation values of the lapse function.[22] The overall sign of the purely imaginary lapse function then tells us whether the relevant saddle point is of the Vilenkin type or of the Hartle-Hawking type. This is important since the different orientation of the Wick rotation may affect the stability of the tensor modes and matter fields [17, 18].

As expected from the semi-classical analysis, we find that the relevant saddle points are of the Vilenkin type for the Dirichlet boundary condition, whereas they become the

[22] This is analogous to ordinary quantum systems, where quantum tunneling is represented by complex trajectories in the real-time path integral [37].

JHEP05(2025)142

saddle points of the Hartle-Hawking type for the Robin boundary condition if the parameter $\tilde{\beta}$ is greater than the critical value. We pointed out, however, that in the case of Robin boundary condition, there is a problem in choosing the integration domain of the lapse function to be the positive real axis since the expectation value of the lapse function tends to vanish unless the scale factor at the final time is large enough. While this can be avoided by extending the integration domain to the whole real axis, it remains to be seen whether this is an acceptable resolution to this issue.

After the quantum tunneling, the real time emerges as one can see from the expectation value of the lapse function that acquires a real part. This happens due to the Stokes phenomenon, in which two saddle points on the imaginary axis merge and split into two in the real direction. Our simulation yields full quantum results, which are consistent with this picture. The complex nature of the lapse function after the quantum tunneling is simply due to the chosen gauge fixing for the time-reparametrization invariance, in which we require that the lapse function be constant in time. We discussed how to obtain an equivalent saddle point configuration with the lapse function that is purely imaginary at early times and purely real at late times.

The saddle-point analysis of the previous work is justified when the cosmological constant $\Lambda = 3H^2$ is small. We have evaluated the expectation value of the lapse function by the H^2 expansion up to the fifth order and find that the perturbative regime is around $H^2 \lesssim 0.1$. This suggests that the perturbative expansion is not valid any more with our choice $H^2 = 1$ for the simulation although the expectation value of the lapse function and hence that of the scale factor turned out to be close to the semi-classical results.

With this capability to perform full quantum calculations, we can investigate various problems in quantum cosmology such as the instability issue of the Vilenkin saddle point by adding the tensor modes and matter fields in the system, which is straightforward. It would be also interesting to perform simulations with different gauge fixing for the time-reparametrization invariance so that one can obtain a real geometry directly as the expectation value. Last but not the least, we consider that quantum cosmology should eventually have a UV completion in string theory. In particular, the simulation results of a nonperturbative formulation of string theory, based on the type IIB matrix model [51], suggest the existence of the transition from Euclidean to Lorentzian geometry at early times [52–54]. In this formulation, there is no need to specify the initial condition since even the time as well as the space emerges dynamically. By comparing with the results obtained in this way, it may be possible to determine the initial boundary condition to be used in quantum cosmology.

Acknowledgments

We would like to thank Masafumi Fukuma, Hikaru Kawai, Jean-Luc Lehners and Kengo Shimada for valuable discussions. The authors are also grateful to Katsuta Sakai and Atis Yosprakob for their help concerning the technique developed in ref. [36]. The computations were carried out on the PC clusters in KEK Theory Center. This work was supported by JST, the establishment of university fellowships towards the creation of science technology innovation, Grant Number JPMJFS2136.

JHEP05(2025)142

A Brief review of the GTM

In this section, we briefly review the GTM [27], which is used in our work in order to overcome the sign problem that occurs in performing Monte Carlo simulations in quantum cosmology. Let us consider a general model

$$Z = \int_{\mathbb{R}^n} dx\, e^{-S(x)} \tag{A.1}$$

with $S \in \mathbb{C}$ and $x \in \mathbb{R}^n$ and define the expectation value of an observable $\mathcal{O}(x)$ as

$$\langle \mathcal{O}(x) \rangle = \frac{1}{Z} \int_{\mathbb{R}^n} dx\, e^{-S(x)} \mathcal{O}(x)\,. \tag{A.2}$$

Since the phase of the complex weight $e^{-S(x)}$ oscillates as a function of x, it is difficult to evaluate the expectation value (A.2) by ordinary Monte Carlo methods for a large system size n, which is nothing but the sign problem.

The basic idea of the GTM is to deform the integration contour in such a way that the phase of the integrand does not oscillate much even for large n. This can be achieved by using the so-called anti-holomorphic gradient flow equation

$$\frac{\partial z_k(x,\tau)}{\partial \tau} = \overline{\frac{\partial S(z(x,\tau))}{\partial z_k}}\,, \tag{A.3}$$

which defines a one-to-one map from $z(x,0) \equiv x \in \mathbb{R}^n$ to $z(x,\tau) \in \mathbb{C}^n$. Due to Cauchy's theorem, the integrals (A.1) and (A.2) remain unaltered under the deformation of the integration contour from $\mathbb{R}^n$ to the n-dimensional real manifold $M_\tau = \{z(x,\tau) | x \in \mathbb{R}^n\}$ embedded in $\mathbb{C}^n$, which implies

$$\langle \mathcal{O}(x) \rangle = \frac{\int_{M_\tau} dz\, e^{-S(z)} \mathcal{O}(z)}{\int_{M_\tau} dz\, e^{-S(z)}}\,. \tag{A.4}$$

Note here that $dz\, e^{-S(z)}$ can be decomposed as

$$\begin{aligned} dz\, e^{-S(z)} &= |dz| e^{i\phi(z)}\, e^{-\mathrm{Re}S(z)} e^{-i\mathrm{Im}S(z)} \\ &= |dz|\, e^{-\mathrm{Re}S(z)} e^{i\theta(z)}\,, \end{aligned} \tag{A.5}$$

where $\phi(z)$ is the phase of dz and $e^{i\theta(z)} \equiv e^{i\phi(z)} e^{-i\mathrm{Im}S(z)}$. Thus the expectation value can be evaluated by Monte Carlo simulation using the reweighting formula as

$$\langle \mathcal{O}(x) \rangle = \frac{\langle e^{i\theta(z)} \mathcal{O}(z) \rangle_\tau}{\langle e^{i\theta(z)} \rangle_\tau}\,, \tag{A.6}$$

where the expectation value $\langle\, \cdot\, \rangle_\tau$ is defined with respect to the partition function

$$Z_\tau = \int_{M_\tau} |dz|\, e^{-\mathrm{Re}S(z)}\,. \tag{A.7}$$

The crucial property of the flow equation (A.3) that enables us to overcome the sign problem is that

$$\frac{\partial S(z(x,\tau))}{\partial \tau} = \frac{\partial S(z(x,\tau))}{\partial z_k} \frac{\partial z_k(x,\tau)}{\partial \tau} = \left| \frac{\partial S(z(x,\tau))}{\partial z_k} \right|^2 \geq 0\,, \tag{A.8}$$

JHEP05(2025)142

which implies that the real part of the action increases along the flow while the imaginary part of the action remains constant. Therefore, most of the points $x \in \mathbb{R}^n$ flow to some points $z(x,\tau) \in \mathbb{C}^n$, for which $\mathrm{Re}S(z)$ is large, and do not contribute to the integral (A.7). The only exceptions are the points $x \in \mathbb{R}^n$ that flow towards some fix points defined by $\frac{\partial S(z)}{\partial z_k} = 0$ since $\mathrm{Re}S(z)$ will not increase much while the points are flowing towards the fixed point. In the $\tau \to \infty$ limit, in particular, M_τ converges to a set of Lefschetz thimbles associated with the fixed points and $\mathrm{Im}S(z)$ is constant on each thimble.[23] In practice, one can just make the flow time τ large enough to make the sign problem under control.

Extra care is needed if multiple thimbles exist since the potential barrier between the regions associated with each thimble tends to diverge as the flow time τ increases, which causes the ergodicity problem at large τ. In order to overcome this problem, one can integrate over the flow time τ by treating it as one of the dynamical variables in the simulation [45]. This is not done in the present work since we can perform meaningful calculations by restricting ourselves to the region associated with one single thimble. As we mentioned at the end of section 4.2, however, if one wishes to sample configurations from both the $N > 0$ and $N < 0$ regions, one needs to implement the integration over the flow time.

Monte Carlo simulation of the model (A.7) can be performed by the HMC algorithm, which uses a fictitious Hamilton dynamics to update the configuration $z(x,\tau)$. There are two different approaches in defining the fictitious Hamilton dynamics. One is to define a fictitious Hamilton dynamics of z constrained on the n-dimensional real manifold M_τ embedded in $\mathbb{C}^n$ [35]. The other is to define a fictitious Hamilton dynamics of $x \in \mathbb{R}^n$ [46]. Let us refer to these approaches as the on-thimble approach and the on-axis approach, respectively, following ref. [36], where pros and cons of each approach are discussed in detail. Here we use the on-thimble approach, which has an advantage that the modulus of the Jacobian for the change of variables associated with the flow is included in the HMC procedure unlike the on-axes approach. The only drawback of the on-thimble approach is that one has to deal with a constrained Hamilton dynamics so that the fictitious time-evolution is constrained to the n-dimensional real manifold M_τ embedded in $\mathbb{C}^n$.

The procedure of the HMC algorithm on the deformed contour M_τ can be summarized as follows [31, 35].

1. Starting from a configuration $z(x,\tau) \in M_\tau$, we generate $\tilde{p} \in \mathbb{C}^n$ with a Gaussian distribution $\propto \exp(-\tilde{p}^2/2)$.

2. We project $\tilde{p}$ onto the tangent space of M_τ at $z(x,\tau)$ as

$$p = J(x,\tau)\,\mathrm{Re}(J^{-1}(x,\tau)\tilde{p}) \tag{A.9}$$

with the Jacobian

$$J_{kl}(x,\tau) = \frac{\partial z_k(x,\tau)}{\partial x_l}\,. \tag{A.10}$$

[23] See ref. [31] for discussions on the residual sign problem coming from the integration measure represented by $\phi(z)$ in (A.5).

3. With the z and p given above, we search for u, $\lambda \in \mathbb{R}^n$ satisfying

$$z_k(x+u,\tau)-z_k(x,\tau)-p_k\Delta s+\frac{\Delta s^2}{2}\frac{\partial \mathrm{Re}S(z(x,\tau))}{\partial z_k}+iJ_{kl}(z(x,\tau))\lambda_l=0\,, \tag{A.11}$$

where Δs is the step size. Then set $x' = x + u$.

4. Define

$$\tilde{p}'_k = \frac{1}{\Delta s}(z_k(x',\tau) - z_k(x,\tau)) - \frac{\Delta s}{2}\frac{\partial \mathrm{Re}S(z(x',\tau))}{\partial z_k} \tag{A.12}$$

and project $\tilde{p}'$ onto the tangent space of M_τ at $z(x',\tau)$ as

$$p' = J(x',\tau)\,\mathrm{Re}(J^{-1}(x',\tau)\tilde{p}')\,. \tag{A.13}$$

5. We repeat the steps 3 to 4 for a fixed number of times, which we denote as n_s.

6. We update the configuration from $z(x,\tau)$ to $z(x',\tau)$ with the probability $\min\left(1, e^{-\Delta H}\right)$, where ΔH is the change of Hamiltonian defined as

$$\Delta H = H(z(x',\tau),p')-H(z(x,\tau),p)\,, \quad \text{where } H(z,p)=\frac{1}{2}p^2+\mathrm{Re}S(z)\,. \tag{A.14}$$

This is the usual Metropolis test in the HMC algorithm, which is needed to guarantee the detailed balance.

The two parameters Δs and n_s in the HMC algorithm can be optimized in the standard manner. First we optimize the step size Δs for fixed $s_\mathrm{f} \equiv n_\mathrm{s}\Delta s$ by maximizing the product $\Delta s \cdot P_\mathrm{acc}(\Delta s)$, where $P_\mathrm{acc}(\Delta s)$ is the acceptance rate of the Metropolis test. Then the total time s_f of the fictitious Hamilton dynamics is optimized by minimizing the computational time needed to obtain a decorrelated configuration. In table 1, we show the parameters used in our simulations.

Simulation results presented in section 5 have been obtained by solving the fictitious Hamilton dynamics 100,000 times and saving the configuration every ten times. As in any Monte Carlo methods, once we generate a set of configurations $\{z^{(j)}\}_{j=1,\ldots,N_\mathrm{conf}}$, we can estimate the expectation value as

$$\langle f(z)\rangle_\tau \approx \frac{1}{N_\mathrm{conf}}\sum_{j=1}^{N_\mathrm{conf}} f(z^{(j)}) \equiv \overline{f(z)}\,. \tag{A.15}$$

Plugging (A.15) into (A.6), one finds

$$\langle \mathcal{O}(z)\rangle \approx \frac{\overline{e^{i\theta(z)}\mathcal{O}(z)}}{\overline{e^{i\theta(z)}}}\,. \tag{A.16}$$

Thus one can obtain the expectation value through (A.16) up to some statistical error, which is of the order of $\mathrm{O}(1/\sqrt{N_\mathrm{conf}})$ if the sampled configurations are separated well enough compared with the autocorrelation time. We estimate the statistical error using the jackknife method, which takes into account the correlation among the sampled configurations.

JHEP05(2025)142

b.c.	H^2	q_f	$\tilde{\beta}/\tilde{\beta}_c$	τ	n_τ	s_f	n_s
D	1	0.8	—	4	40	0.1	15
D	1	10	—	4	40	0.38	10
R	1	10	0.3	4	40	0.39	10
R	1	10	1.2	6	60	0.4	10
R	0.3	10	1.2	5	50	0.25	10
R	0.1	10	1.2	5	50	0.25	20
R	0.03	10	1.2	5	70	0.2	30

Table 1. The parameters for the HMC simulation by the GTM are presented. The D and R in the first column represent the Dirichlet and Robin boundary conditions, respectively, at the initial time. In the fifth and sixth columns, we show the parameters used in solving the flow equation, where τ represents the total flow time and n_τ represents the number of steps. In the last two columns, we show the parameters used in the HMC algorithm, where $s_\mathrm{f} = n_\mathrm{s}\Delta s$ represents the total time of the fictitious Hamilton dynamics and n_s represents the number of steps used in solving the Hamilton equation.

Next we discuss a technical problem with the flow equation (A.3), which was pointed out recently in ref. [36]. For that, let us define the Hessian of the action as

$$H_{kl} = \frac{\partial^2 S(z)}{\partial z_k \partial z_l}\,, \tag{A.17}$$

and consider the singular value decomposition of the symmetric matrix H,

$$H = U^T D\, U\,, \tag{A.18}$$

where U is a unitary matrix and $D = \mathrm{diag}(d_1, \ldots, d_n)$ is a real positive diagonal matrix. Then, the stiffness of the system can be defined as $\eta(H) = \frac{d_n}{d_1}$. High stiffness makes the effect of the flow equation very different for each mode, which causes difficulty in the simulation.[24]

In order to solve this problem, we have used a new technique [36], which introduces a "preconditioner" in the flow equation as

$$\frac{\partial}{\partial \tau} z_k(x,\tau) = A_{kl} \overline{\frac{\partial S(z(x,\tau))}{\partial z_l}}\,, \tag{A.19}$$

where A should be a positive-definite hermitian matrix in order to keep the crucial property (A.8) of the flow equation intact. Making use of this freedom, we can optimize the stiffness ($\eta(\bar{A}H) = 1$) by choosing

$$A(z,\bar{z}) = U^\dagger D^{-1} U = (\bar{H}(\bar{z}) H(z))^{-\frac{1}{2}}\,. \tag{A.20}$$

When we solve the flow equation numerically, we discretize the flow equation using the so-called "Runge-Kutta 4" method.

[24] This problem occurs, in particular, when we choose the parameter $\tilde{\beta}$ in the Robin boundary condition at the initial time to be $\tilde{\beta} > \tilde{\beta}_\mathrm{c}$.

JHEP05(2025)142

B Derivation of the effective action at finite ϵ

In this section, we derive the effective action (5.2) for the lapse function N at finite ϵ, which is used in obtaining the perturbative expansion (5.6). It is useful to consider first the case of Dirichlet boundary condition with $q(0) = q_{\rm i}$ left arbitrary.

Let us start from the discretized partition function (4.2). Solving the classical equation of motion (4.4) with the boundary condition $q_0 = q_{\rm i}$ and $q_n = q_{\rm f}$, we get

$$q_k = q_{\rm i} + k(k+1)\epsilon^2 N^2 + C\,\frac{k}{n}\,, \qquad \text{where } C = q_{\rm f} - q_{\rm i} - n(n+1)\epsilon^2 N^2\,. \tag{B.1}$$

We can integrate out q_k $(k = 1, \cdots, (n-1))$ by just performing the Gaussian integral, which amounts to plugging the classical solution in the action and getting the factors $(\sqrt{N})^{n-1}$. Thus we obtain

$$Z = \int dN\, N^{-1/2}\, e^{iS_{\rm eff}^{(\rm D)}/H^2}\,, \tag{B.2}$$

$$S_{\rm eff}^{(\rm D)} = -\frac{\pi^2}{2}\left\{\epsilon^2 N^3 - N^3 + 6N(q_{\rm f} + q_{\rm i} - 2) + \frac{3}{N}(q_{\rm f} - q_{\rm i})^2\right\}\,, \tag{B.3}$$

up to an irrelevant constant. The finite ϵ effect appears only as an $\mathrm{O}(\epsilon^2)$ term in the effective action (B.3), and we retrieve (2.15) in the $\epsilon \to 0$ limit.

In the case of Robin boundary condition, we start from the discretized partition function (4.10). The integration over q_k except for q_0 can be readily done as in the Dirichlet case. Thus we are left with the integration over $q_0 = q_{\rm i}$ given by

$$Z = \int dN\, N^{-1/2} \int dq_{\rm i}\, e^{i\{S_{\rm eff}^{(\rm D)} + (\alpha q_{\rm i} + \frac{1}{2\beta}(q_{\rm i})^2\}/H^2}\,. \tag{B.4}$$

Extracting the terms that depend on $q_{\rm i}$, we get

$$S_{\rm eff} = \frac{N - 3\pi^2\beta}{2\beta N}(q_{\rm i})^2 + \left\{\frac{3\pi^2}{N}(q_{\rm f} - N^2) + \alpha\right\} q_{\rm i}\,. \tag{B.5}$$

The Gaussian integral over $q_{\rm i}$ yields an extra factor $\sqrt{N/(N - 3\pi^2\beta)}$. Thus we arrive at

$$Z = \int dN\, (N - 3\pi^2\beta)^{-1/2} e^{iS_{\rm eff}^{(\rm R)}/H^2}\,, \tag{B.6}$$

$$S_{\rm eff}^{(\rm R)} = -\frac{\pi^2}{2}\left[\epsilon^2 N^3 + \frac{\beta N\left\{\frac{3\pi^2}{N}(q_{\rm f} - N^2) + \alpha\right\}^2}{\pi^2(N - 3\pi^2\beta)} - \left\{N^3 - 6N(q_{\rm f} - 2) - \frac{3}{N}(q_{\rm f})^2\right\}\right]\,, \tag{B.7}$$

which leads to (5.2). In the $\epsilon \to 0$ limit, we retrieve the result (2.26) in the continuum.

Data Availability Statement. This article has no associated data or the data will not be deposited.

Code Availability Statement. This article has no associated code or the code will not be deposited.

JHEP05(2025)142

References

[1] A. Vilenkin, *Creation of Universes from Nothing*, *Phys. Lett. B* **117** (1982) 25 [INSPIRE].

[2] A. Vilenkin, *Quantum Creation of Universes*, *Phys. Rev. D* **30** (1984) 509 [INSPIRE].

[3] A. Vilenkin, *Approaches to quantum cosmology*, *Phys. Rev. D* **50** (1994) 2581 [gr-qc/9403010] [INSPIRE].

[4] J.B. Hartle and S.W. Hawking, *Wave Function of the Universe*, *Phys. Rev. D* **28** (1983) 2960 [INSPIRE].

[5] J.-L. Lehners, *Review of the no-boundary wave function*, *Phys. Rept.* **1022** (2023) 1 [arXiv:2303.08802] [INSPIRE].

[6] J. Maldacena, *Comments on the no boundary wavefunction and slow roll inflation*, arXiv:2403.10510 [INSPIRE].

[7] J.J. Halliwell and J. Louko, *Steepest Descent Contours in the Path Integral Approach to Quantum Cosmology. 1. The De Sitter Minisuperspace Model*, *Phys. Rev. D* **39** (1989) 2206 [INSPIRE].

[8] G.W. Gibbons, S.W. Hawking and M.J. Perry, *Path Integrals and the Indefiniteness of the Gravitational Action*, *Nucl. Phys. B* **138** (1978) 141 [INSPIRE].

[9] J. Feldbrugge, J.-L. Lehners and N. Turok, *Lorentzian Quantum Cosmology*, *Phys. Rev. D* **95** (2017) 103508 [arXiv:1703.02076] [INSPIRE].

[10] J. Diaz Dorronsoro et al., *Real no-boundary wave function in Lorentzian quantum cosmology*, *Phys. Rev. D* **96** (2017) 043505 [arXiv:1705.05340] [INSPIRE].

[11] J. Diaz Dorronsoro et al., *Damped perturbations in the no-boundary state*, *Phys. Rev. Lett.* **121** (2018) 081302 [arXiv:1804.01102] [INSPIRE].

[12] J.J. Halliwell, J.B. Hartle and T. Hertog, *What is the No-Boundary Wave Function of the Universe?*, *Phys. Rev. D* **99** (2019) 043526 [arXiv:1812.01760] [INSPIRE].

[13] H.-Y. Chen, Y. Hikida, Y. Taki and T. Uetoko, *Complex saddles of three-dimensional de Sitter gravity via holography*, *Phys. Rev. D* **107** (2023) L101902 [arXiv:2302.09219] [INSPIRE].

[14] H.-Y. Chen, Y. Hikida, Y. Taki and T. Uetoko, *Complex saddles of Chern-Simons gravity and dS_3/CFT_2 correspondence*, *Phys. Rev. D* **108** (2023) 066005 [arXiv:2306.03330] [INSPIRE].

[15] H.-Y. Chen, Y. Hikida, Y. Taki and T. Uetoko, *Semiclassical saddles of three-dimensional gravity via holography*, *Phys. Rev. D* **110** (2024) 026018 [arXiv:2403.02108] [INSPIRE].

[16] H.-Y. Chen, Y. Hikida, Y. Taki and T. Uetoko, *The semi-classical saddles in three-dimensional gravity via holography and mini-superspace approach*, *JHEP* **07** (2024) 283 [arXiv:2404.10277] [INSPIRE].

[17] J. Feldbrugge, J.-L. Lehners and N. Turok, *No smooth beginning for spacetime*, *Phys. Rev. Lett.* **119** (2017) 171301 [arXiv:1705.00192] [INSPIRE].

[18] J. Feldbrugge, J.-L. Lehners and N. Turok, *No rescue for the no boundary proposal: Pointers to the future of quantum cosmology*, *Phys. Rev. D* **97** (2018) 023509 [arXiv:1708.05104] [INSPIRE].

JHEP05(2025)142

[19] A. Vilenkin and M. Yamada, *Tunneling wave function of the universe*, *Phys. Rev. D* **98** (2018) 066003 [arXiv:1808.02032] [INSPIRE].

[20] A. Vilenkin and M. Yamada, *Tunneling wave function of the universe II: the backreaction problem*, *Phys. Rev. D* **99** (2019) 066010 [arXiv:1812.08084] [INSPIRE].

[21] J. Feldbrugge, J.-L. Lehners and N. Turok, *Inconsistencies of the New No-Boundary Proposal*, *Universe* **4** (2018) 100 [arXiv:1805.01609] [INSPIRE].

[22] H. Matsui, S. Mukohyama and A. Naruko, *No smooth spacetime in Lorentzian quantum cosmology and trans-Planckian physics*, *Phys. Rev. D* **107** (2023) 043511 [arXiv:2211.05306] [INSPIRE].

[23] H. Matsui and S. Mukohyama, *Hartle-Hawking no-boundary proposal and Hořava-Lifshitz gravity*, *Phys. Rev. D* **109** (2024) 023504 [arXiv:2310.00210] [INSPIRE].

[24] H. Matsui, *No smooth spacetime: Exploring primordial perturbations in Lorentzian quantum cosmology*, *Phys. Rev. D* **110** (2024) 023503 [arXiv:2404.18609] [INSPIRE].

[25] A. Di Tucci and J.-L. Lehners, *No-Boundary Proposal as a Path Integral with Robin Boundary Conditions*, *Phys. Rev. Lett.* **122** (2019) 201302 [arXiv:1903.06757] [INSPIRE].

[26] A. Di Tucci, J.-L. Lehners and L. Sberna, *No-boundary prescriptions in Lorentzian quantum cosmology*, *Phys. Rev. D* **100** (2019) 123543 [arXiv:1911.06701] [INSPIRE].

[27] A. Alexandru et al., *Sign problem and Monte Carlo calculations beyond Lefschetz thimbles*, *JHEP* **05** (2016) 053 [arXiv:1512.08764] [INSPIRE].

[28] E. Witten, *Analytic Continuation Of Chern-Simons Theory*, *AMS/IP Stud. Adv. Math.* **50** (2011) 347 [arXiv:1001.2933] [INSPIRE].

[29] AURORASCIENCE collaboration, *New approach to the sign problem in quantum field theories: High density QCD on a Lefschetz thimble*, *Phys. Rev. D* **86** (2012) 074506 [arXiv:1205.3996] [INSPIRE].

[30] M. Cristoforetti, F. Di Renzo, A. Mukherjee and L. Scorzato, *Monte Carlo simulations on the Lefschetz thimble: Taming the sign problem*, *Phys. Rev. D* **88** (2013) 051501 [arXiv:1303.7204] [INSPIRE].

[31] H. Fujii et al., *Hybrid Monte Carlo on Lefschetz thimbles — A study of the residual sign problem*, *JHEP* **10** (2013) 147 [arXiv:1309.4371] [INSPIRE].

[32] R. Loll, *Quantum Gravity from Causal Dynamical Triangulations: A Review*, *Class. Quant. Grav.* **37** (2020) 013002 [arXiv:1905.08669] [INSPIRE].

[33] D. Jia, *Complex, Lorentzian, and Euclidean simplicial quantum gravity: numerical methods and physical prospects*, *Class. Quant. Grav.* **39** (2022) 065002 [arXiv:2110.05953] [INSPIRE].

[34] D. Jia, *Truly Lorentzian quantum cosmology*, *Phys. Rev. D* **108** (2023) 103540 [arXiv:2211.00517] [INSPIRE].

[35] M. Fukuma, N. Matsumoto and N. Umeda, *Implementation of the HMC algorithm on the tempered Lefschetz thimble method*, arXiv:1912.13303 [INSPIRE].

[36] J. Nishimura, K. Sakai and A. Yosprakob, *Preconditioned flow as a solution to the hierarchical growth problem in the generalized Lefschetz thimble method*, *JHEP* **07** (2024) 174 [arXiv:2404.16589] [INSPIRE].

[37] J. Nishimura, K. Sakai and A. Yosprakob, *A new picture of quantum tunneling in the real-time path integral from Lefschetz thimble calculations*, *JHEP* **09** (2023) 110 [arXiv:2307.11199] [INSPIRE].

JHEP05(2025)142

[38] C. Teitelboim, *Quantum Mechanics of the Gravitational Field*, *Phys. Rev. D* **25** (1982) 3159 [INSPIRE].

[39] C. Teitelboim, *Causality Versus Gauge Invariance in Quantum Gravity and Supergravity*, *Phys. Rev. Lett.* **50** (1983) 705 [INSPIRE].

[40] C. Teitelboim, *The Proper Time Gauge in Quantum Theory of Gravitation*, *Phys. Rev. D* **28** (1983) 297 [INSPIRE].

[41] B. Banihashemi and T. Jacobson, *On the lapse contour in the gravitational path integral*, *Phys. Rev. D* **111** (2025) 066014 [arXiv:2405.10307] [INSPIRE].

[42] M. Honda, H. Matsui, K. Okabayashi and T. Terada, *Resurgence in Lorentzian quantum cosmology: No-boundary saddles and resummation of quantum gravity corrections around tunneling saddle points*, *Phys. Rev. D* **110** (2024) 083508 [arXiv:2402.09981] [INSPIRE].

[43] M. Ailiga, S. Mallik and G. Narain, *Lorentzian Robin Universe*, *JHEP* **01** (2024) 124 [arXiv:2308.01310] [INSPIRE].

[44] M. Ailiga, S. Mallik and G. Narain, *Lorentzian Robin Universe of Gauss-Bonnet Gravity*, *Gen. Rel. Grav.* **57** (2025) 29 [arXiv:2407.16692] [INSPIRE].

[45] M. Fukuma and N. Matsumoto, *Worldvolume approach to the tempered Lefschetz thimble method*, *PTEP* **2021** (2021) 023B08 [arXiv:2012.08468] [INSPIRE].

[46] G. Fujisawa, J. Nishimura, K. Sakai and A. Yosprakob, *Backpropagating Hybrid Monte Carlo algorithm for fast Lefschetz thimble calculations*, *JHEP* **04** (2022) 179 [arXiv:2112.10519] [INSPIRE].

[47] J.-L. Lehners, *Wave function of simple universes analytically continued from negative to positive potentials*, *Phys. Rev. D* **104** (2021) 063527 [arXiv:2105.12075] [INSPIRE].

[48] E. Witten, *A Note On Complex Spacetime Metrics*, arXiv:2111.06514 [INSPIRE].

[49] C. Jonas, J.-L. Lehners and J. Quintin, *Uses of complex metrics in cosmology*, *JHEP* **08** (2022) 284 [arXiv:2205.15332] [INSPIRE].

[50] T. Hertog, O. Janssen and J. Karlsson, *Kontsevich-Segal Criterion in the No-Boundary State Constrains Inflation*, *Phys. Rev. Lett.* **131** (2023) 191501 [arXiv:2305.15440] [INSPIRE].

[51] N. Ishibashi, H. Kawai, Y. Kitazawa and A. Tsuchiya, *A large N reduced model as superstring*, *Nucl. Phys. B* **498** (1997) 467 [hep-th/9612115] [INSPIRE].

[52] J. Nishimura, *Signature change of the emergent space-time in the IKKT matrix model*, *PoS* **CORFU2021** (2022) 255 [arXiv:2205.04726] [INSPIRE].

[53] K.N. Anagnostopoulos et al., *Progress in the numerical studies of the type IIB matrix model*, *Eur. Phys. J. ST* **232** (2023) 3681 [arXiv:2210.17537] [INSPIRE].

[54] M. Hirasawa et al., *The effects of SUSY on the emergent spacetime in the Lorentzian type IIB matrix model*, *PoS* **CORFU2023** (2024) 257 [arXiv:2407.03491] [INSPIRE].

JHEP05(2025)142